International Journal of Plasticity 168 (2023) 103684

Contents lists available at ScienceDirect

International Journal of Plasticity

journal homepage: www.elsevier.com/locate/ijplas

Interaction of extended dislocations with nanovoid clusters

Ashley M. Roach [a,*], Shuozhi Xu [b], Darby J. Luscher [c], Daniel S. Gianola [a], Irene J. Beyerlein [a,d]

[a] Materials Department, University of California, Santa Barbara, CA 93106-5050, USA
[b] School of Aerospace and Mechanical Engineering, University of Oklahoma, Norman, OK 73019-1052, USA
[c] Theoretical Division, Los Alamos National Laboratory, Los Alamos, NM 87545, USA
[d] Department of Mechanical Engineering, University of California, Santa Barbara, CA 93106-5070, USA

ARTICLE INFO

Keywords:
Dislocations
Strengthening mechanisms
Voids and inclusions
Inhomogeneous metallic material
Phase-field dislocation dynamics

ABSTRACT

Voids of nanoscale dimensions in irradiated metals can act as obstacles to dislocation motion and cause strengthening. In this work, nanovoid strengthening and the influences of void size, void spacing and material properties, such as stacking fault energies, on dislocation bypass mechanisms are investigated using Phase Field Dislocation Dynamics, a three-dimensional mesoscale model that predicts the minimum energy pathway taken by discrete dislocations. A broad range of face centered cubic metals (copper, nickel, silver, rhodium, and platinum) and nanovoid sizes and spacings are treated, altogether spanning void size–to–dislocation stacking fault width ratios from less than unity to ten. Material γ-surfaces, calculated from *ab initio* methods, are input directly into the formulation. The analysis reveals that the critical bypass stress scales linearly with the linear void fraction, effective isotropic shear modulus, and ratio of the intrinsic to unstable stacking fault energies. With only a few exceptions, the critical stress is controlled by the stress required for the leading partial to impinge the voids (to move within range of the attractive image stress field of the void). When the void diameter is nearly an order of magnitude greater than the stacking fault width, the mechanism determining critical strength shifts to the stress for the dislocation to breakaway after partially cutting the void. This situation corresponds to that treated by line tension models and is realized here for Pt, with a sub-nanometer stacking fault width.

1. Introduction

Irradiated metals have unique damage considerations, with local regions that can have very high concentrations of nanovoids and other nanoscale defects, such as point defects and dislocation loops (Zinkle and Matsukawa, 2004; Wang et al., 2018, 2019; Liu et al., 2020; Chen and Song, 2022). Voids traditionally studied, usually submicron in size or larger, act as stress concentrators that grow and coalesce, eventually causing severe damage or even failure (Sills and Boyce, 2020; Liu et al., 2021; Christodoulou et al., 2021). However, nanoscale voids can instead act as obstacles to dislocation motion (Scattergood and Bacon, 1982; Dérès et al., 2015; Bergner et al., 2015; Li et al., 2016), resulting in strengthening reminiscent of precipitation strengthening behavior (Fan et al., 2022). Thus, the presence of such nanoscale defects in irradiated metal can cause strengthening, altering its behavior from that expected in its original design (Lucas, 1993; Li et al., 2012).

Nanovoids may not necessarily be isolated or dilute across the material, but can be generated in clusters, where local void spacing is also nanoscale in dimension (Huang et al., 2015; Skoczeń and Ustrzycka, 2016). Nanovoids can develop in all types of nuclear

* Corresponding author.
E-mail address: amroach@ucsb.edu (A.M. Roach).

https://doi.org/10.1016/j.ijplas.2023.103684
Received 3 March 2023; Received in revised form 14 June 2023
Available online 1 July 2023
0749-6419/© 2023 Published by Elsevier Ltd.

relevant metals, such as those with body centered cubic (bcc) structures, such as W or Ta (Fukuda et al., 2016; Bao et al., 2022), or face centered cubic (fcc) crystals, like Cu and Ni alloys (Singh and Evans, 1995; Xu et al., 2020b) or stainless steels (Lucas, 1993; Huang et al., 2015). They are especially prevalent in the latter since the surface energy in fcc metals is exceedingly low (Wen and Zhang, 2007). Dislocations in fcc metals can be extended, with core widths nearly as wide as the nanovoids with which they interact (Hunter et al., 2014), suggesting more complex dislocation-void considerations.

As many of these dislocation-void interactions cannot be seen directly in-situ, simulations are called upon to predict how these interactions could proceed. These have traditionally included analytical modeling, atomistic simulations, and mesoscale calculations. As a proxy for understanding bulk yielding behavior, many modeling methods have focused on the critical stress for a single gliding dislocation to bypass a nanovoid or linear array of equally spaced nanovoids. Convenient, analytical models have emerged that relate the critical stress to bypass with geometric length scales of the void array. One of the earliest models (Scattergood and Bacon, 1982) is based on the elastic line tension of a perfect dislocation segment piercing voids to a certain depth while the remaining segments proceed to bow out in the material space between voids. The critical bypass stress was controlled by the stress for the dislocation to "break away" from the void and corresponds to a critical bow out angle. The critical stress scales directly with the isotropic-effective shear modulus μ, Burgers vector magnitude b, and $ln\left(\bar{D}\right)$, where $\bar{D}$ is the harmonic mean of the void diameter D and array spacing S, given by

$$\bar{D} = \frac{1}{\frac{1}{D} + \frac{1}{S}}. \tag{1}$$

In more recent times, Crone et al. (2015) evolved the line tension model to fit calculations that more wholly considered image forces. Functional forms were fitted to data from DD simulations that included complexities arising from elastic anisotropy, image forces acting on dislocation segments sufficiently close to the void surface(s), self-interaction considerations for a bowing dislocation segment, and the inherent stress concentration field due to the presence of a void in a material under external load. This led to $\tau_{c_{analytical}} = \frac{\mu b}{2\pi L_{eff}} ln\left(\bar{D}\right)$, where L_{eff} is the critical distance between intersection points on neighboring voids when the dislocation reaches the maximum bowing angle. Additional work in bcc W (Wu et al., 2022) has built upon these analytical models in DDD to investigate the hardening of a 3D random array of void clusters.

As mentioned earlier, dislocations in metals with an fcc structure are extended in the glide plane. They dissociate into Shockley partial dislocations tethered together by an extended region of local hcp ordering, or a stacking fault. The stacking fault width (SFW) is inversely proportional to the material intrinsic stacking fault energy (SFE), defined as the energy penalty associated with creating the stacking fault between partials. Atomistic approaches can capture this Shockley partial dissociation in fcc metals. A number of studies (Hatano and Matsui, 2005; Osetsky and Bacon, 2005; Bacon and Osetsky, 2005; Osetsky and Bacon, 2010; Simar et al., 2011; Okita et al., 2014; Xiong et al., 2015; Xu et al., 2019a) have used molecular dynamics (MD) or Concurrent Atomistic-Continuum (CAC) methods to examine in detail the steps taken as dissociated dislocations shear and overcome nanovoid obstacles. They observe a positive correlation between obstacle strength and nanovoid D, although the influence of D is often coupled with varying S (and hence different $\bar{D}$). In Cu and Ni (Hatano and Matsui, 2005; Osetsky and Bacon, 2005; Bacon and Osetsky, 2005; Simar et al., 2011), a shift in bypass mechanisms is observed to be generally sensitive to the void size, D, in relation to the SFW of the extended dislocations. When D shifts from being smaller than the dynamic SFW to being larger a change in shearing mechanisms is often observed, though the exact transition D varies. Generally, the critical obstacle strength shifts from being controlled by the trailing partial to the leading partial. In these studies, however, the influence of SFW or SFE among different fcc metals was not the objective of the investigation.

A few MD studies have aimed to isolate the role of SFE in nanovoid strengthening (Asari et al., 2013; Okita et al., 2014; Doihara et al., 2018; Hayakawa et al., 2019). In these studies, a range of SFE were artificially varied in a Cu parent interatomic potential, with all other material properties held constant. Doing so overcomes the difficulty in creating equally reliable interatomic potentials for different fcc metals, albeit with the loss of the concurrent influence of all other properties, like lattice parameter and elastic constants. They concluded that nanovoid obstacle strength is positively correlated with SFE, as well as other geometric considerations such as where voids are bisected by the glide plane (Okita et al., 2014). Similar mechanism shifts from trailing partial to leading partial dominated were again observed, now with a dependence on both D and SFE, as well as a higher-energy simultaneous partial shearing mechanism (Doihara et al., 2018).

Like atomistic calculations, mesoscale or analytical dislocation models have also proven valuable for lending insight into dislocation interactions with nanoscale obstacles. For dislocations, "mesoscale" implies access to longer time and/or length scales than atomistic techniques, while still retaining the effects of dislocation stress fields and line character. Among these mesoscale dislocation models, Phase Field Dislocation Dynamics (PFDD) (Beyerlein and Hunter, 2016; Xu, 2022) is a 3D, real-space technique that predicts the pathways taken by dislocations with little to no rules or adjustable parameters. PFDD can treat longer dislocations over longer glide distances interacting with more defects than typically considered in atomistic calculations. All material parameter inputs can be obtained either via experimental measurement or density functional theory (DFT), limiting the use of empirical potentials. PFDD enables representation of the dissociated core structure of dislocations in fcc metals, through the incorporation of γ-surfaces from DFT (Xu et al., 2019b; Hunter et al., 2014), and multiple phases in the same crystal (Xu et al., 2022b), such as voids in a crystalline matrix. Thus, for this study, PFDD was chosen as the model framework because it can account for the discreteness of the dislocation, the extended core structure, and elastic anisotropy. Here, we can apply it to evaluate a broad set of fcc metals and void geometries with input from a consistent method without additional concerns of the varying degrees of reliability of interatomic potentials. Previously, the PFDD model was used by Zeng et al. (2019) to predict alloy strengthening from nanoscale particles of SFE lower than the matrix, building upon the (Hirsch and Kelly, 1965) stacking fault strengthening theory. They observed

a size effect in peak strengthening for particle sizes approaching that of the average equilibrium SFW. PFDD was recently advanced to model void cutting by moving dislocations (Xu et al., 2022a), where the authors investigated the critical stress for dislocations to bypass a variety of nanoscale obstacles, including voids and both shearable and unshearable precipitates in Cu (fcc) and Nb (bcc).

In this work, we use PFDD to investigate the interaction between long extended dislocations in fcc metals and an array of nanovoids under an applied load. The idealized regular array is intended to represent a localized, highly concentrated region of nanovoids in an irradiated fcc crystal that dislocations originating from the surrounding bulk encounter. Five metals, Ag, Cu, Ni, Pt, and Rh, are treated with material property input, γ-surfaces and elastic constants from the same *ab initio* method. Calculations are performed to reveal the extent to which stacking fault energies affect the critical stress to bypass an array of nanovoids and the relationship between this critical stress and the geometry of the void array. To the authors' knowledge, this is the first time a mesoscale model has been applied to study the interaction of extended dislocation cores with nanovoids that incorporates the role of material property variations, such as fault energies and anisotropic elasticity, known to affect core structure. It is revealed that in most cases, in which the void sizes range from less than to greater than the extended core width, the critical stress occurs when the sum total stress exerted on the dislocation during bowing equals that of the attractive image force of the void surface. This contrasts with the conventional model for perfect dislocations, in which the stress for the dislocation to breakaway from the void determines the critical stress. With the leading partial controlling bypass, the critical stress scales linearly with the ratio of the intrinsic to unstable stacking fault energies, and directly scales with the linear void fraction. A few cases with Pt, with a very fine core ($\sim$ 1 nm), suggest that the bypass mechanism transitions to one similar to that of a perfect dislocation when the void diameter is an order of magnitude greater than the width of the dislocation core.

This paper is structured as follows. We begin with a review of the PFDD method for biphase materials, with a focus on voids, and summarize the metals treated here and relevant material input for them in Section 2. Section 3 presents findings on dislocation/void interactions, including the sequence of events for shearing, critical stresses, and effects of SFE. In Section 4, the results are discussed in comparison to line tension models and atomistic methods. An empirical model for the relationship between the critical stress and material parameters, as identified by the calculations, is presented. Section 5 summarizes the salient findings of this work.

2. Material and methods

2.1. PFDD formulation

We first present the PFDD formulation for a biphase medium, containing two crystalline materials, 1 and 2, with different elastic properties and fault energies. This is a brief account and more details can be found in Xu et al. (2022a,b). These simulations were performed without thermal fluctuations, but this is expected to have minimal influence on fcc dislocation bypass behavior (Bacon and Osetsky, 2005).

As with phase-field formulations, order parameters are introduced for the non-conserved variables that evolve. Let $\boldsymbol{\phi}$ be the set of order parameters and ϵ^{v} the virtual strain tensor. For each slip system α, the order parameter $\phi_\alpha = 0$ and 1 represents the unslipped and slipped states, respectively. In the general formulation, dislocations can glide in material 1 and material 2, provided that they are both crystalline.

The total energy density ψ consists of four terms: elastic energy density ψ_{ela}, lattice energy density ψ_{lat}, gradient energy density ψ_{gra}, and external energy density ψ_{ext} (Xu et al., 2020a), i.e., at each point $\boldsymbol{x}$,

$$\psi(\boldsymbol{x}) = \psi_{\mathrm{ela}}(\boldsymbol{x}) + \psi_{\mathrm{lat}}(\boldsymbol{x}) + \psi_{\mathrm{gra}}(\boldsymbol{x}) - \psi_{\mathrm{ext}}(\boldsymbol{x}). \tag{2}$$

For a biphase medium, the total elastic strain energy, ψ_{ela}, consists of the sum of two terms. The first is the energy density of the "equivalent", homogeneous system without the inhomogeneity, $\psi^{\mathrm{eq}}_{\mathrm{ela}}(\boldsymbol{x})$, and the second is the difference in energy density between the inhomogeneous and homogeneous systems, dubbed the "extra" elastic energy density, $\psi^{\mathrm{ex}}_{\mathrm{ela}}(\boldsymbol{x})$ (Xu et al., 2022a), i.e.,

$$\psi_{\mathrm{ela}}(\boldsymbol{x}) = \psi^{\mathrm{eq}}_{\mathrm{ela}}(\boldsymbol{x}) + \psi^{\mathrm{ex}}_{\mathrm{ela}}(\boldsymbol{x}) \tag{3}$$

where

$$\psi^{\mathrm{eq}}_{\mathrm{ela}}(\boldsymbol{x}) = \frac{1}{2}[\boldsymbol{\epsilon}(\boldsymbol{x}) - \boldsymbol{\epsilon}^0(\boldsymbol{x})] \cdot \boldsymbol{C}[\boldsymbol{\epsilon}(\boldsymbol{x}) - \boldsymbol{\epsilon}^0(\boldsymbol{x})] \tag{4}$$

$$\psi^{\mathrm{ex}}_{\mathrm{ela}}(\boldsymbol{x}) = \frac{1}{2}\boldsymbol{\epsilon}^{\mathrm{v}}(\boldsymbol{x}) \cdot \boldsymbol{M}^{[2]}(\boldsymbol{x})\boldsymbol{\epsilon}^{\mathrm{v}}(\boldsymbol{x}) \tag{5}$$

where we note that $\psi^{\mathrm{ex}}_{\mathrm{ela}}$ exists only in material 2. In the above expression, the 4th order tensor $\boldsymbol{M}$ is modulus associated with the elastic strain energy due to the presence of the inhomogeneity, i.e.,

$$M^{[2]}_{ijkl}(\boldsymbol{x}) = -C^{[1]}_{ijmn}\left[C^{[2]}_{mnpq}(\boldsymbol{x}) - C^{[1]}_{mnpq}\right]^{-1} C^{[1]}_{pqkl} - C^{[1]}_{ijkl} \tag{6}$$

Additionally, $\boldsymbol{C}$ is the elasticity tensor and $\boldsymbol{\epsilon} = \mathrm{sym}\boldsymbol{\beta}$ is the strain tensor, where $\boldsymbol{\beta} = \nabla\boldsymbol{u}$ is the distortion with $\boldsymbol{u}$ being the displacement, and $\boldsymbol{\epsilon}^0$ is the eigenstrain tensor, i.e.,

$$\boldsymbol{\epsilon}^0(\boldsymbol{x}) = \begin{cases} \boldsymbol{\epsilon}^{\mathrm{p}}(\boldsymbol{x}), & \boldsymbol{x} \in \text{material 1} \\ \boldsymbol{\epsilon}^{\mathrm{p}}(\boldsymbol{x}) + \boldsymbol{\epsilon}^{\mathrm{v}}(\boldsymbol{x}), & \boldsymbol{x} \in \text{material 2} \end{cases} \tag{7}$$

where $\boldsymbol{\epsilon}^{\mathrm{p}}$ and $\boldsymbol{\epsilon}^{\mathrm{v}}$ are the plastic strain tensor and virtual strain tensor, respectively. The tensor $\boldsymbol{\epsilon}^{\mathrm{p}}$ is related to plastic distortion tensor $\boldsymbol{\beta}^{\mathrm{p}}$, and then to the order parameter $\boldsymbol{\phi}$, i.e.,

$$\boldsymbol{\epsilon}^{\mathrm{p}} = \mathrm{sym}\boldsymbol{\beta}^{\mathrm{p}} \tag{8}$$

$$\boldsymbol{\beta}^{\mathrm{p}}(\boldsymbol{\phi}) = \sum_{\alpha=1}^{n_{\mathrm{op}}} \frac{b_\alpha \phi_\alpha}{d_\alpha} \boldsymbol{s}_\alpha \otimes \boldsymbol{n}_\alpha \tag{9}$$

where n_{op} is the total number of order parameters, $\boldsymbol{s}_\alpha$ the slip direction unit vector, b_α the slip vector magnitude, $\boldsymbol{n}_\alpha$ the slip plane unit normal, and d_α the interplanar spacing between two adjacent slip planes, for slip system α. Although the model permits an arbitrary number of slip systems, for the goals of this work it is only necessary to focus on one slip system.

Besides ψ_{ela}, the other three energy densities in (2) are

$$\psi_{\mathrm{lat}}(\boldsymbol{x}) = \frac{\gamma_{\mathrm{gsf}}^{[N]}(\boldsymbol{\phi}(\boldsymbol{x}))}{l_{\mathrm{gsf}}^{[N]}(\boldsymbol{x})} \tag{10}$$

$$\psi_{\mathrm{gra}}(\boldsymbol{x}) = \sum_{\alpha,\beta=1}^{n_{\mathrm{sp}}} \eta_{\alpha\beta}^{[N]} \nabla\phi_\alpha(\boldsymbol{x}) \cdot \boldsymbol{\Xi}_{\alpha\beta}(\boldsymbol{x}) \nabla\phi_\beta(\boldsymbol{x}) \tag{11}$$

$$\psi_{\mathrm{ext}}(\boldsymbol{x}) = \boldsymbol{\sigma}_{\mathrm{app}} \cdot \boldsymbol{\epsilon}^0(\boldsymbol{x}) \tag{12}$$

where $N = 1$ or 2, denoting different materials, $\gamma_{\mathrm{gsf}}^{[N]}$ is the generalized stacking fault energy (GSFE) (Xu et al., 2019b), $l_{\mathrm{gsf}}^{[N]}$ is the spacing between the two adjacent slip planes based on which $\gamma_{\mathrm{gsf}}^{[N]}$ is calculated, $\eta_{\alpha\beta}^{[N]}$ is the gradient energy coefficient for the order parameter sets $\alpha\beta$ in material N (Xu et al., 2019c), $\boldsymbol{\sigma}_{\mathrm{app}}$ is the applied stress tensor, and

$$\boldsymbol{\Xi}_{\alpha\beta} = \frac{\boldsymbol{b}_\alpha \cdot \boldsymbol{b}_\beta}{d_\alpha d_\beta} [(\boldsymbol{n}_\alpha \cdot \boldsymbol{n}_\beta)\boldsymbol{I} - \boldsymbol{n}_\beta \otimes \boldsymbol{n}_\alpha] \tag{13}$$

where $\boldsymbol{I}$ is the identity tensor.

Once the energy functional is set and the order parameters initialized, the total system energy is minimized with respect to each order parameter ϕ_α and each virtual strain component ϵ_{ab} (where $a, b = 1, 2, 3$) via the time-dependent Ginzburg–Landau (TDGL) equation, i.e.,

$$\dot{\phi}_\alpha(\boldsymbol{x}) = -m_0[\partial_{\phi_\alpha(\boldsymbol{x})}(\psi_{\mathrm{ela}}(\boldsymbol{x}) + \psi_{\mathrm{lat}}(\boldsymbol{x}) - \psi_{\mathrm{ext}}(\boldsymbol{x})) - \nabla \cdot \partial_{\nabla\phi_\alpha(\boldsymbol{x})}\psi_{\mathrm{gra}}(\boldsymbol{x})] \tag{14}$$

$$\dot{\epsilon}_{ab}^{\mathrm{v}}(\boldsymbol{x}) = -m_0^{\mathrm{v}}\partial_{\epsilon_{ab}^{\mathrm{v}}(\boldsymbol{x})}(\psi_{\mathrm{ela}}(\boldsymbol{x}) - \psi_{\mathrm{ext}}(\boldsymbol{x})) \tag{15}$$

where the superposed dot denotes the time derivative. The Ginzburg–Landau coefficients m_0 and m_0^{v} are not necessarily the same but should both be non-negative. Note that (14) is applied to both materials while (15) is applied to only material 2.

Lastly, to properly consider the short-range dislocation/void interactions, we treat a void as a second crystalline phase with a set of non-zero order parameters and exceedingly low elastic moduli, generalized stacking fault energies, and zero gradient energy coefficients, where prior work has confirmed bypass stress convergence with these values (Xu et al., 2022a,b), i.e.,

$$C_{ijkl}^{\mathrm{void}} = C_{ijkl}^{\mathrm{matrix}}/10^5, \quad \gamma_{\mathrm{gsf}}^{\mathrm{void}} = \gamma_{\mathrm{gsf}}^{\mathrm{matrix}}/10^5, \quad \eta_{\alpha\beta}^{\mathrm{void}} = 0 \tag{16}$$

Representing the inhomogeneity of the void as an eigenstrain of an equivalent problem (Lei et al., 2013) enables an accurate representation of the stress field produced by the void under far-field loading, and the elastic moduli mismatch between the matrix and void creates image forces on dislocations in the vicinity of the void surface.

2.2. PFDD model setup

Fig. 1 illustrates the simulation cell used here. It contains a [110]-type edge dislocation dipole on a (111)-type plane. Each dislocation has the same line type but opposite Burgers vector direction to force net zero displacement of a Burgers loop around the cell. Periodic boundary conditions are applied to all three directions, and dipole placement centers the two dislocations equidistant from each other across the cell, as well as over the periodic boundary to guarantee initial equilibrium of interaction forces. On each half of the cell a linear periodic array of voids, oriented parallel to the dislocation line direction, are placed in the path of each dipole and equidistant from their respective dislocation and the cell boundary to minimize the influence of inherent stress fields on the initial dissociation response. A non-zero cell height into and out of the slip plane allows for 3D spherical voids bisected by the (111) plane. Dislocation slip is confined to the (111) plane.

The material is oriented with x defined as $[1\bar{1}0]$, y as $[11\bar{2}]$, and z as [111]. When expressed in terms of the Burgers vector b, the grid spacing is $0.50b$ in x, $0.87b$ in y, and $0.82b$ in z. This is done to maximize compute time efficiency, but results in the voids being slightly ellipsoidal. The simulation cell dimensions range between 768–2048 voxels along x, alternate between 128, 256, or 384 voxels along y, and are 64 voxels along z. Dimensions along x are varied to prevent bowing dislocations from interacting across the periodic boundaries, and are varied along y to achieve desired void obstacle spacings. The FFT simulation approach involves a regular grid of voxels. As such, a minimum void size is set by the number of voxels needed to form an adequately spherical void — below this size limit nanovoids are more cuboidal than spherical.

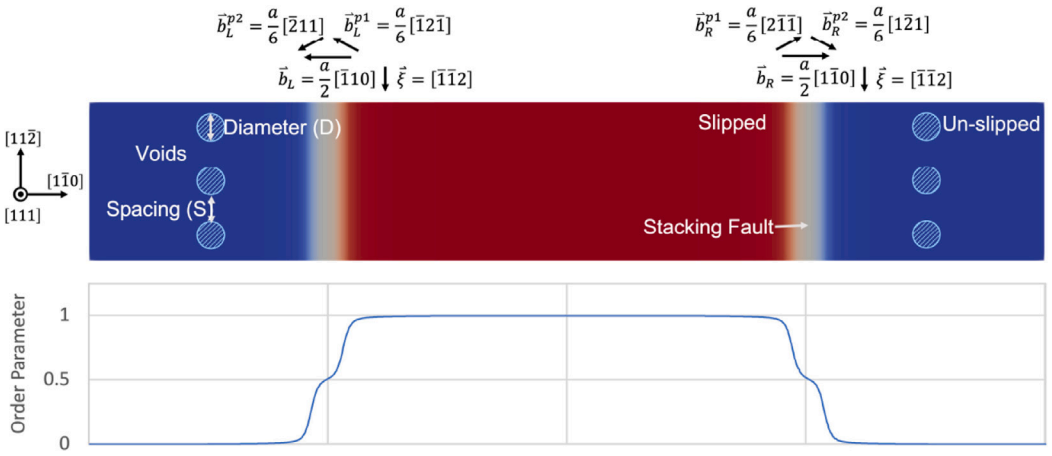

Fig. 1. General simulation cell and dislocation dipole with an example void array. The slip plane is (111) and dislocations are edge character with perfect Burgers vectors. Both dislocations have dissociated into two partials. The left one $[\bar{1}10]$ dissociates into $[\bar{1}2\bar{1}]$ and $[\bar{2}11]$, and the right one $[1\bar{1}0]$ dissociates into $[2\bar{1}\bar{1}]$ and $[1\bar{2}1]$. External shear stress is applied perpendicular to the dislocation line direction, causing the dislocations to shear away from each other and towards the voids. The cell is colored in blue (un-slipped regions), red (slipped regions) and white (stacking fault regions). Below is a plot of the plastic strain order parameter across the length of the cell, tracking the shearing progress of the dislocation dipole as external stress is applied. Slipped regions are indicated by an order parameter of 1, un-slipped by an order parameter of 0, and the intermediate 0.5 are stacking faults. (For interpretation of the references to color in this figure legend, the reader is referred to the web version of this article.)

Table 1
Nanovoid sizes and spacings in the linear arrays considered here.

Obstacle label	Void size D (b)	Void spacing S (b)	Void fraction F (%)
D6F6	6.1	104.8	5.5
D6F13	6.1	49.4	10.9
D6F26	6.1	21.7	21.9
D6F41	6.1	12.4	32.8
D6F60	6.1	5.0	54.7
D8F6	7.8	103.0	7.0
D8F13	7.8	47.63	14.1
D8F26	7.8	19.9	28.1
D8F41	7.8	10.7	42.2
D8F60	7.8	6.1	56.3
D16F13	16.5	94.4	14.8
D16F26	16.5	39.0	29.7
D16F41	16.5	20.5	44.5
D16F60	16.5	11.3	59.4
D25F13	25.1	224.3	11.3
D25F26	25.1	85.7	22.7
D25F41	25.1	30.3	45.3
D25F60	25.1	11.8	68.0

Void sizes D ranging from 6-25b were chosen, Table 1, with spacings S ranging from $\approx$ 5–300b. D and S are intended to be both smaller and larger than the SFW of the dislocations in the metals modeled here. Our D and S ranges were informed by ranges measured from experiment (Li et al., 2012; Bergner et al., 2015), and chosen to encompass and extend beyond the ranges tested in atomistics (Hatano and Matsui, 2005; Simar et al., 2011; Asari et al., 2013; Osetsky and Bacon, 2010). These values correspond to linear void fractions of $\approx$ 5–60%, and different nanovoid obstacle geometries have similar void fractions with different void diameters. Linear void fraction F in Table 1 is defined as the fraction of void space present along the line of obstacles,

$$F = \frac{D}{D+S}. \tag{17}$$

The naming convention for void arrays in Table 1 is as follows: void diameter grouping is given as "DX", with X in units of (b), and void fraction grouping as "FY", where Y is the target linear void fraction F in percent. Due to computational efficiency, for the two largest void sizes, D16 and D25, the smallest F is F13. Actual F values vary from target "FY" families because of geometric constraints on allowable cell size dimensions; the FFT solver requires the cell y dimension to be a multiple of the z dimension, limiting available intervals of S.

Under a prescribed external shear stress the system is allowed to evolve to a minimum energy state. For each simulation, this shear stress is constant and does not evolve. Next, the stress is incrementally increased to identify the critical stress, measured as

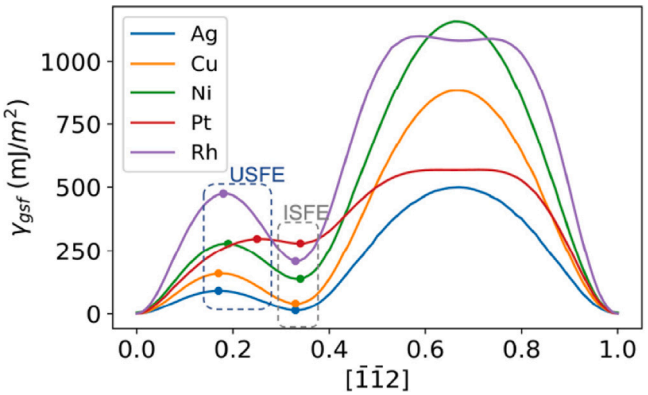

Fig. 2. γ-surfaces from density functional theory (DFT) within the (111) plane along the general partial dislocation direction [$\bar{1}\bar{1}$2] for all five materials in this study.
Source: Replotted from Figure 2 of Su et al. (2019).

the value between the increment that moves the dislocation and one increment below, where it does not move. This critical stress is first identified for a dislocation in a void-free crystal to move three lattice vectors, and for the sake of brevity this is called the zero-temperature Peierls stress $\tau_{peierls}$.[1] The critical bypass stress for a void obstacle, τ_c, is defined similarly but with the nanovoids present. The stress increments used for determining these critical stresses are refined until $\tau_{peierls}$ and τ_c have a maximum error of ±10MPa. To minimize periodic image effects, the dimensions of the cell are varied along x to reach converged $\tau_{peierls}$ and τ_c for all materials and void obstacle geometries.

Lastly, the locations of the leading and trailing partials are tracked. Their core positions are defined by projecting the disregistry fields, ζ_1 and ζ_2, along the partial Burgers vectors, Eqs. (18) and (19) as follows (Xu et al., 2019b)

$$\zeta^1_{partial} = \zeta_1 cos\left(30°\right) + \zeta_2 sin\left(30°\right) \tag{18}$$

$$\zeta^2_{partial} = \zeta_1 cos\left(30°\right) - \zeta_2 sin\left(30°\right) \tag{19}$$

where ζ_1 and ζ_2 are the disregistry fields oriented parallel and perpendicular to the perfect dislocation Burgers vector, respectively. The disregistry is defined as the difference between the in-plane displacement above and below the glide plane caused by the presence of a dislocation (Hunter et al., 2011). A dislocation is located at the boundary where the disregistry changes from 0 to 1. The location of a partial corresponds to where its projection equals $\zeta^X_{partial}$ of $\frac{\sqrt{3}}{4}b$ (Xu et al., 2019b). Disregistry fields are related to order parameters through $\zeta_\beta = \int_{\alpha=1}^{n_{sp}} \phi_\alpha \boldsymbol{b}_\alpha \cdot \boldsymbol{s}_\beta$, where n_{sp} is the number of order parameters within a slip plane, $\boldsymbol{b}_\alpha$ is the Burgers vector of order parameter α, and $\boldsymbol{s}_\beta$ is the slip direction vector component in the direction β.

The distance between the partial cores and the void surfaces can be calculated at each y-slice along the simulation cell. By fitting a spline to the dislocation segment localized around each void obstacle, a tangent angle at each y-slice of the cell is measured and the bowing angle evolution explicitly monitored (see Fig. 3d for schematic illustration).

2.3. Material parameters

Five pure fcc transition metals are chosen: platinum (Pt), silver (Ag), copper (Cu), rhodium (Rh), and nickel (Ni). These metals vary widely in their intrinsic stacking fault energies (ISFE or SFE) and unstable stacking fault energies (USFE) (Fig. 2). PFDD incorporates the entire γ-surface and as such can replicate the dissociation of fcc dislocations in Shockley partials (Beyerlein and Hunter, 2016). γ-surfaces are input from density functional theory (DFT) (Su et al., 2019) and are unique for each material. The ISFE/USFE ratios are reported in Table 2 to enable better cross-material comparison. For example, Pt has a very shallow GSFE minimum compared to all other fcc metals chosen, suggesting a reduced driving force to fully dissociate. An artificial material, platinum-copper or Pt_{Cu}, was also created by swapping the Cu γ-surface into the Pt material to investigate the influence of this shallow GSFE minimum. The equilibrium SFW varies inversely (Hunter et al., 2014) with ISFE. Stress-free, or equilibrium, SFW values for edge dislocations, calculated from PFDD by taking the distance between partial core locations found with Eqs. (18) and (19) in a stress-free cell, are given in Table 2 along the [1$\bar{1}$0] Burgers vector direction in the (111) plane.

The master energy functional used here in PFDD includes a gradient coefficient input parameter unique to each material. Eq. (11), a gradient energy term, is used to characterize the energy density of the dislocation core, and a coefficient $\eta^{[N]}_{\alpha\beta}$ must be applied to this term to anchor this core structure to a physical value. Molecular Statics (MS) results of the dissociated fcc dislocations are

[1] It is recognized that the Peierls stress has been rigorously defined as the stress required for a dislocation to move one lattice vector (Schoeck, 2001; Peierls, 1940) and varies depending on the computational or analytical approach used.

Table 2
Stacking fault energies from DFT γ-surfaces and zero-stress equilibrium stacking fault widths calculated from PFDD.

Metal	Intrinsic SFE (mJ/m^2)	ISFE/USFE ratio (unitless)	Stacking fault width (b)
Silver	14.49	0.16	17.67
Copper	41.83	0.28	10.99
Rhodium	208.67	0.44	5.73
Nickel	152.13	0.51	4.98
Platinum	280.87	0.94	2.17

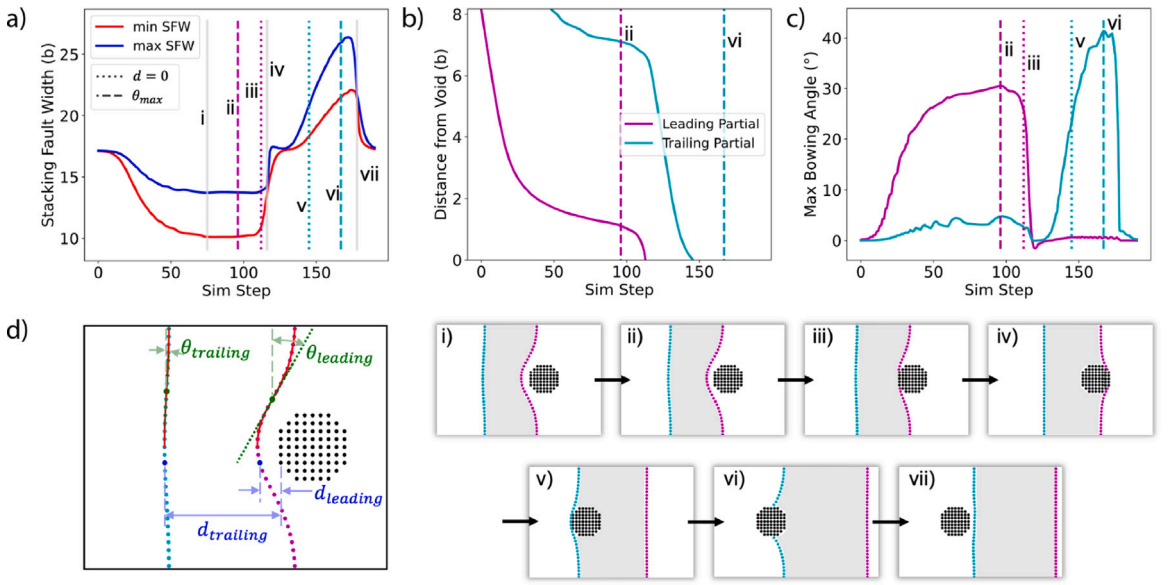

Fig. 3. General shearing sequence for representative case of D8F26 (see Table 1) in Cu for the right dipole (shears left to right). Voids are black, the leading partial is magenta and the trailing partial is cyan. Fluctuations in SFW along the extended dislocation line are tracked in (a). The distance between the partial dislocation core centers and the leftmost edge of the voids are tracked in (b), where the point of minimum distance to the void is located in (d), as a blue dot, for each partial. Maximum bowing angles at each simulation step are tracked in (c). A spline, in red, is fit to each partial in (d) to locate and measure the point of max bowing. All (a)-(c) are plotted versus every 200th simulation timestep. The timestep Δt is normalized by $\Delta t = m_0 \mu \Delta t_{real}$ where m_0 is the mobility coefficient (Eq. (14)), and Δt_{real} the real time. In (a)-(c), significant steps are indicated with snapshots given in i-vii: (i) approximate start to crawling period, (ii) maximum bowing angle for leading partial, (iii) leading partial contact with void surface, (iv) leading partial shears void, (v) trailing partial contact with void surface, (vi) trailing partial maximum bowing angle, and (vii) trailing partial shears void. (For interpretation of the references to color in this figure legend, the reader is referred to the web version of this article.)

used for comparison, and the gradient coefficient is identified as that which enables the PFDD calculated dislocation core to agree with the MS core. In this work, the gradient coefficient was adjusted until the MS and PFDD dislocations had equivalent partial dislocation core widths, measured using Eq. (20) adapted from Xu et al. (2019b) for the case of $\beta = 1$,

$$l_1 = \frac{|\,\zeta_1(+\infty) - \zeta_1(-\infty)\,|}{|\,\partial_x \zeta_1(x=0)\,|} \tag{20}$$

The partial core is measured along ζ_1 (parallel with Burgers vector, $\beta = 1$). The value $\zeta_1(+\infty)$ is the disregistry at the transition from the unslipped region ($\zeta_1 = 0$) to the partial, and $\zeta_1(-\infty)$ is at the transition from the partial to the stacking fault region. The value $\partial_x \zeta_1(x=0)$ is at maximum slope for ζ_1.

Lastly, other material properties are required, such as the full elastic modulus tensor and lattice vector, as reported in Table 3. Modulus values were taken from Warlimont and Martienssen (2018), with cubic symmetry applied to the tensor. Isotropic shear modulus, calculated with the Voigt average (Voigt, 1889) rewritten as Equation 36 in Xu et al. (2019d), is reported in Table 3 for material comparisons. Finally, the Zener Anisotropy Ratio $2C_{44}/(C_{11} - C_{12})$ and Burgers vector magnitude in nanometers are summarized for the chosen metals.

With all intricacies considered, a typical run-time for these simulations is on the order of 1–10 days and depends on cell size and material, and not the number of dislocations. In past work, it has been demonstrated that the PFDD code can be made multiple times faster using GPUs, if larger cell sizes are of interest (Eghtesad et al., 2018).

Table 3
Elastic anisotropic constants, isotropic effective shear modulus, Zener ratio and Burgers vector for the studied metals.

Metal	C11 (GPa)	C12 (GPa)	C44 (GPa)	Shear modulus μ (GPa)	Zener anisotropy ratio	Burgers vector (nm)
Silver	122	92	45.5	33.3	3.03	0.29366
Copper	169	122	75.3	54.6	3.20	0.25696
Rhodium	413	194	184	154.2	1.68	0.27089
Nickel	247	153	122	92.0	2.60	0.24883
Platinum	347	251	76.5	65.1	1.59	0.28058

3. Results

3.1. Dislocation-void interaction behavior across several metals

3.1.1. Shearing sequence for Ag, Cu, Ni and Rh

In this section, we examine the interactions with a void array for dislocations in Ag, Ni, Cu, and Rh. For these metals, the dislocation first dissociates into two Shockley partials before gliding towards the voids. Pt is treated separately in the next section because, while the dislocation dissociates into a leading and trailing partial, the SFW in Pt is much narrower than the other metals (2.17*b*) and boundaries between the partials and intervening stacking fault are diffuse.

Fig. 3 tracks the right dislocation of the dipole with the D8F26 void array as a representative case. To capture the entire shearing sequence, the applied stress in this case corresponds to the τ_c, where the dissociated dislocation can approach and cut through the voids and glide away. In Fig. 3a, the minimum and maximum SFW values along the length of the extended dislocation are tracked. Fig. 3b tracks the position of the leading partial with respect to the closest void surface as it moves towards the void array, illustrated in Fig. 3d. The bowing angles are measured from a straight dislocation position as shown in Fig. 3d, and Fig. 3c tracks the maximum bowing angles along the lines for the leading and trailing partials as the shearing sequence evolves.

In under-driven conditions, when the applied stress is just below τ_c, the dislocation first glides towards the array under the externally applied shear stress. The dislocation arrests at a finite distance from the void surface corresponding to step i (Fig. 3i). Depending on the material, the trailing partial either remains straight or bows with a lower bowing angle than the lead partial. The leading partial is still continuous, as no part of its line has sheared the voids, yet its line morphology is wavy bowing around the voids. The instantaneous SFW has compressed below the starting SFW, particularly in the regions where a void is located directly in the path.

When the stress is raised to the τ_c, the leading and trailing partials start to move, but only minimally. This begins the *crawling period*, over which the extended dislocation maintains a steady, relatively slow velocity towards the voids that is much slower than the initial approach. During this time, repulsive long-range forces due to the void are counteracted by the partials bowing. While the two partials are crawling towards the voids, the leading partial bowing angle increases, but at a slower pace as well. It reaches its maximum at step ii (Fig. 3ii). The crawling period ends when the leading partial comes within the so-called *capture radius* of the void, where the dislocation is attracted under the image stress of the void (Anderson et al., 2017) and, together with the dislocation bowing, overpowers the repulsive Peach-Koehler forces. This capture radius is very fine in dimension and varies mildly among the metals and void array geometries, within 0.5–1.5b. As this is a meso-scale technique, this distance is on the order of the spatial resolution of the model and a rigorous quantification of the capture radius is not possible. However we observe that this capture radius is inversely proportional to isotropic shear modulus, and shows a dependency on void geometry.

Once within this radius, the leading partial accelerates towards the void and begins to shear it (Fig. 3iii). Almost immediately afterwards, the leading partial fully shears the void array (Fig. 3iv) and the trailing partial moves forward to also pierce the void array (Fig. 3v) with no detectable delay. The bowing angle of the trailing partial continues to increase as its shears the void until its maximum bowing angle is reached (Fig. 3vi). Finally after fully shearing the void array, the extended dislocation straightens (Fig. 3vii) and the SFW is then restored to that before it encountered the nanovoids.

Our simulation results show that this basic sequence of events for the leading and trailing partials applies to all four metals and all studied void array geometries. The peak stress in this sequence corresponds to the stress needed to push the leading partial within the capture radius of the void, after which it immediately impinges the void. Thus, τ_c is controlled by the leading partial impingement stress and not the leading partial or trailing partial breakaway stresses after contact. A few MD studies considering the intersection of an extended dislocation in Cu and Ni (Hatano and Matsui, 2005; Osetsky and Bacon, 2005; Bacon and Osetsky, 2005; Simar et al., 2011) for certain void geometries reported a bypass mechanism similarly controlled by the leading partial. They found a sensitivity to the void diameter in relation to the SFW to an extent that varied slightly among studies. Here, the dislocation subtly constricts before cutting the void and each partial bows under the external stress when it cuts the void, as shown in Fig. 3ii for the leading and Fig. 3vi for the trailing partials. The maximum bowing angles of the partials can reach angles in excess of 30–60 degrees, depending on material and obstacle geometry. For this study, the range of metals and void arrays altogether cover situations in which the void sizes or spacings vary from less than and close to the SFW to around ten times the SFW (see Tables 1 and 2). Thus, for a wide range of *D* and SFW, the leading partial impingement remains the controlling mechanism by which the dislocation bypasses the void array.

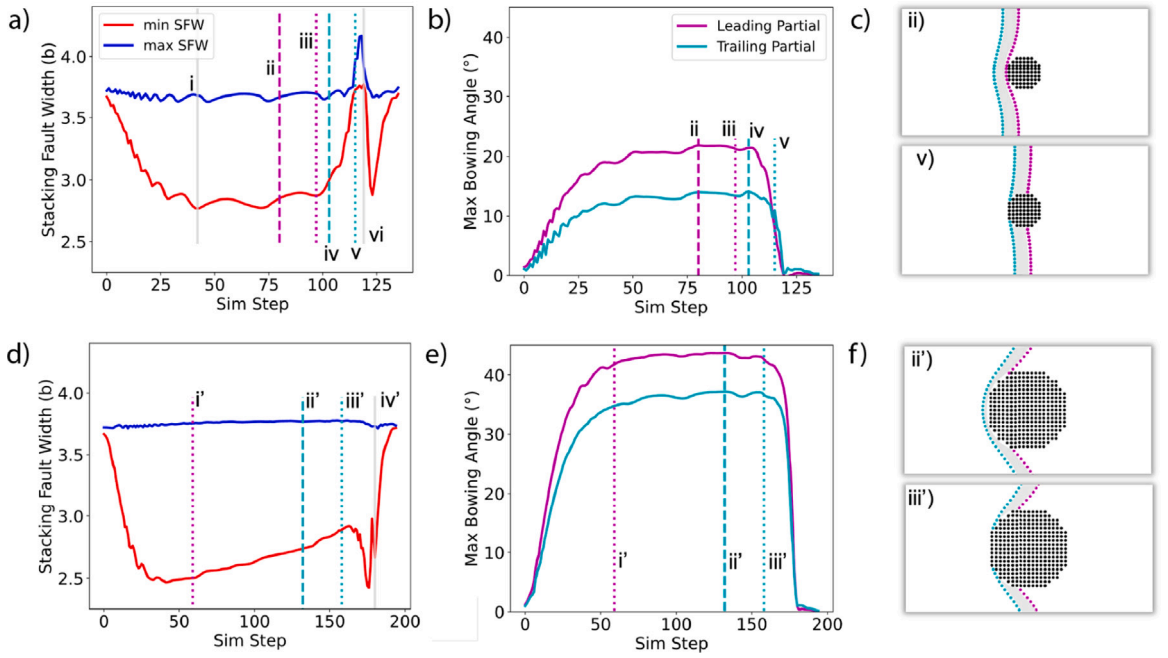

Fig. 4. Detailed shearing sequence in Pt. For D8F26 void obstacle, (a) gives fluctuations in SFW along the dislocation line, (b) shows the max bowing angles of each partial at each simulation step, and two significant simulation snapshots are given in (c). Snapshot (ii) is the max bowing angle of the leading partial and (v) is the trailing partial piercing the void. Additional steps of interest identified in (a) are (i) start to an abbreviated crawling period, (iii) leading partial void piercing, (iv) trailing partial max bowing, (vi) full obstacle shearing. For the D16F26 void obstacle, (d) tracks the SFW, (e) tracks the bowing angle, and (f) gives two significant simulation snapshots for (ii') the maximum bowing angle of both partials and (iii') trailing void piercing. Additional simulation steps of interest in (d) are (i') leading partial void piercing, and (iv') full shearing.

3.1.2. *Shearing sequence for platinum*

Fig. 4 shows the shearing sequence in Pt at the τ_c. A few characteristics distinct from those of the other metals are observed. First, the interaction depends on void size. With the smaller void sizes, i.e., D6 and D8, the leading and trailing partial follow the same motion. The two partials slow as they near the voids, although an extended crawling period could not be perceived as in the other metals. The leading partial achieves a maximum bowing angle (Fig. 4c, snapshot ii), followed by the trailing partial. Afterwards they shear the void rapidly as a unit. The capture radius was not discernible by tracking the distance between partials and the closest void surface. The τ_c is instead controlled by the stress needed for both partials to approach and first shear the void together. This critical step is similar to that of the other tested metals, except both partials act together, with SFW varying $\approx 1b$ in the process.

With larger void sizes, D16 and D25, simulations reveal that the critical step has changed. In under-driven conditions below τ_c the leading partial dislocation is able to cut into the void, while the trailing partial stays behind. In this state, the bowing angles of both partials increase. The dislocation then fully arrests. At τ_c, both the leading and trailing partials bow out simultaneously and their bowing angles reach a global maximum at which point the trailing partial also cuts the void. Immediately, the partials fully shear the void. Afterwards, the extended dislocation straightens and restores the SFW prior to encountering the voids. Thus, for larger nanovoids, τ_c is controlled by the stress needed for the partials to breakaway from the void after the leading partial has already partially sheared it. This is similar to what has been proposed by conventional dislocation/void models (Crone et al., 2015) and in some instances in MD for dissociated dislocations (Simar et al., 2011), though only for the leading partial in this study.

3.2. *Critical stress and void fraction*

Fig. 5 shows the critical stress τ_c needed to fully cut through the voids versus the linear void fraction F. All measured τ_c are normalized by isotropic shear modulus μ to enable comparison of trends across different materials. While it is expected that larger void sizes would require higher τ_c, the linear relationship with F across all materials and void sizes is remarkable. Void fraction F encompasses in one measure two characteristic length scales: void size and void spacing. This result implies nanovoid strengthening depends on void diameter and spacing but only through their combined effects on void fraction, without any additional independent influences on τ_c. As another advantage, void fraction F can be measured via microscopy.

Of significance, the coefficient of the linear relationship found in Fig. 5a depends on the material. To help assess the material dependence, Fig. 5c plots the calculated linear regression slopes with the effective isotropic shear modulus $\mu/100$ for each metal. The strong scaling reveals the importance of μ, with arguably the exception of Pt. The increased scatter around the linear regression curve for Pt in Fig. 5a suggests a higher-order dependence of τ_c on void size beyond what is captured in F. Fig. 5b confirms this, with τ_c - F slopes varying between void size data sets.

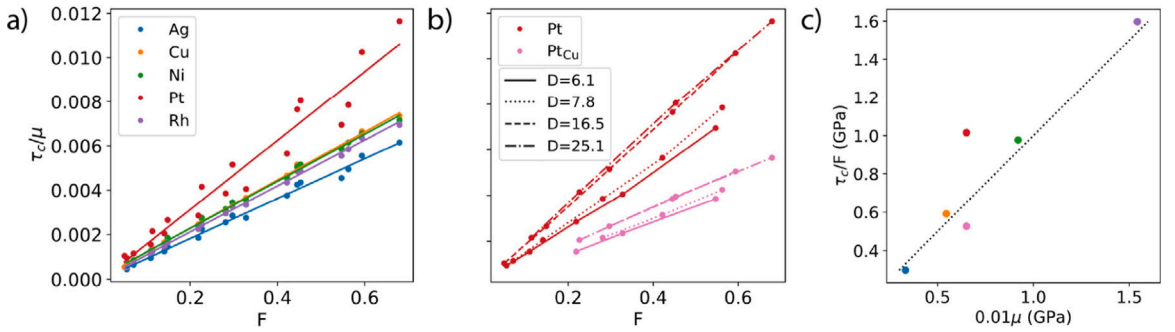

Fig. 5. τ_c/μ versus 1D void fraction F (Eq. (17)) for all materials. In (a) all void diameter data sets, shown as bullet points, collapse to a single curve taken as a simple linear regression of the data. The exception is Pt, where higher order void size dependencies are evidenced by increased spread in data points. (b) shows Pt data grouped by void size data sets compared with the artificial platinum-copper material, Pt_{Cu}, for which all data sets have collapsed to a single shared slope. In (c) linear regression slopes, calculated from a τ_c (GPa) versus F plot, are plotted against a scaled isotropic shear modulus μ (GPa), showing good agreement with all materials but Pt and, to a lesser extent, the artificial Pt_{Cu}. The dashed line represents $y = x$ to illustrate the extent of agreement between regression slopes and scaled 0.01μ.

As we have seen, Pt has a unique dislocation core compared to the other metals tested, and as a result it undergoes a different interaction with the nanovoids. Instead of discrete, well-defined Shockley partials separated by a stacking fault, Pt has a very narrow SFW, and consequently more closely resembles an un-dissociated (compact) dislocation. Further, the shear across the SFW is diffuse, spread with no sharp boundaries between the intrinsic fault and the two partials. This results from its distinct γ-surface compared to the other metals. As seen in Table 2, Pt has the unique characteristic of an $ISFE/USFE$ ratio nearing unity, indicating a reduced driving force to dissociate. To isolate the role of the Pt core, a calculation was repeated for a hypothetical "platinum-copper" material, or Pt_{Cu}, in which the Pt γ-surface was swapped for Cu. Apart from the γ-surface, this artificial Pt_{Cu} has all material properties of Pt. The dislocation in Pt_{Cu} is extended, with a distinct stacking fault width of $12.8b$ between the two Shockley partials. As shown in Fig. 5b, τ_c for Pt_{Cu} scales linearly with F, and no higher order void size dependencies are apparent, in agreement with all other fcc materials studied. In Fig. 5c, it is observed that Pt_{Cu}, with an artificially extended dislocation introduced by swapping in the Cu γ surface, aligns more closely with other metals in the trend of τ_c/F vs μ than actual Pt. Thus, the deviation in this trend observed for Pt results from its weakly dissociated core. This also implies that the extended core structure underpins the strong linear τ_c - F relationship seen in Fig. 5a.

4. Discussion

4.1. Role of void array geometry in nanovoid strengthening

We have found a strong role of void geometry represented by F on τ_c that is not anticipated by conventional analytical models to date. Before probing material dependencies in our results, the performance of the geometric scaling of some analytical models is examined. We recall from the Scattergood and Bacon (SB) and Crone Munday and Knapp (CMK) analytical models, a geometric parameter $\bar{D}$ (Eq. (1)) was proposed to combine the effects of spacing and size of an obstacle array into a single term. Fig. 6a compares the calculated critical stresses, τ_c, versus $\bar{D}$ from the SB analytical model. Following the analytical model formulation, the stress plotted τ_c^{SB} is normalized by the unitless parameter of combined material and void geometry properties ($\tau_c^{SB} = (\tau_c/\mu)(S/b)$). On this semi-log plot, the SB model predicts a linear relationship, yet no such relationship is observed in the simulation results of this study. Rather the scaling varies not only with materials but also length scales of the void array.

Fig. 6b compares the scaling relationship of the CMK model with the τ_c values calculated here. In accordance with the CMK formulation, we plot $\tau_c^{CMK} = (\tau_c/\mu)((S+R)/b)$ versus $\bar{D}$, where $R = D/2$ is the void radius, all in units of b. For all materials and all void array geometries, no perceptible trend or master curve emerges. Data for each material is grouped by void size, and a strong void size dependence (or void size effect) is observed, where τ_c^{CMK} is inversely related to $\bar{D}$ within each D grouping. Overall the critical stresses increase with increasing D across sets, though there is no continuity across void size data sets contrary to the CMK model.

4.2. Critical stress and material properties

4.2.1. ISFE

An important material parameter not taken into account in most dislocation/nanovoid interaction models is the intrinsic stacking fault energy. Our study of a suite of fcc metals provides the opportunity to identify the role of SFE on τ_c to bypass nanovoids. Fig. 7 shows τ_c/μ versus ISFE and SFW for a representative case of void size $D = 7.8b$. A weak positive trend is observed for τ_c/μ versus ISFE, and a moderate inverse trend for τ_c/μ versus SFW. These relationships are marginally strengthened with increasing F. A Spearman's rank correlation coefficient of ≈ 0.63 for ISFE and ≈ -0.75 for SFW confirm these observations. The spread inherent in each material data set is more dominant than the positive or inverse trends with material properties, suggesting changing void obstacle geometry F has a much stronger impact than changing SFE.

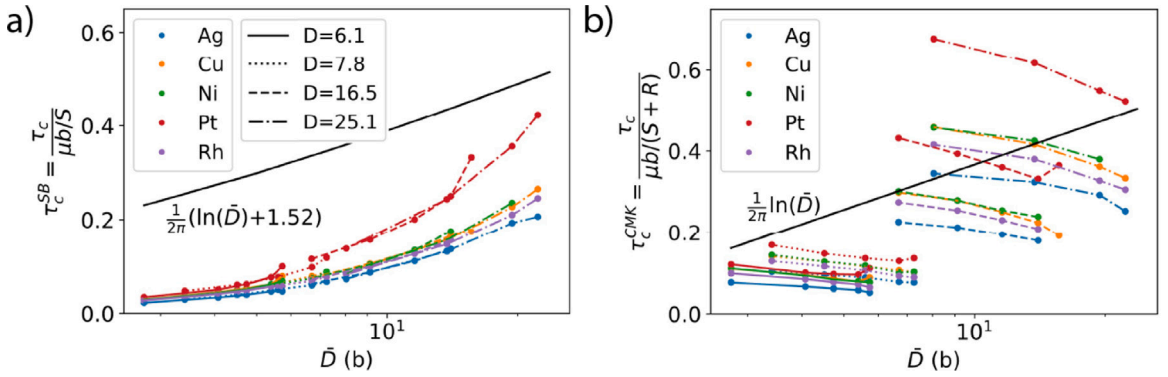

Fig. 6. Analytical solutions plotted together with PFDD data, colored by material and grouped by void size data sets, on a logarithmic $\bar{D}$ scale in units of b, where (a) the Scattergood and Bacon (SB) solution for voids is in black with the equation given below for offset $\Delta = 1.52$ for voids (Scattergood and Bacon, 1982). Critical stress values are normalized by $(\mu b/S)$. In (b) the analytical solution from Crone Munday and Knapp (CMK) is in black with the equation above, and critical stress values are normalized by $(\mu b/S+R)$.

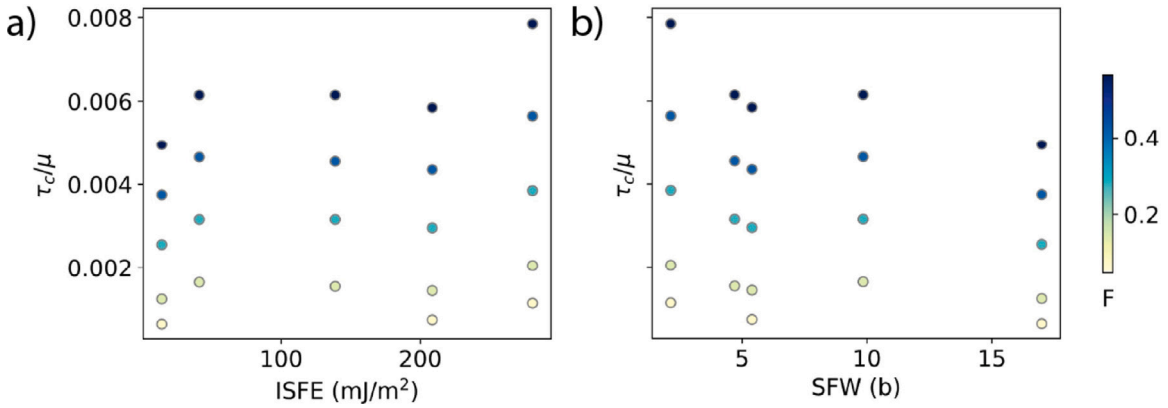

Fig. 7. τ_c/μ for a representative void size $D = 7.8b$ plotted versus (a) Intrinsic Stacking Fault Energy (ISFE) in (mJ/m^2), and (b) static Stacking Fault Width (SFW) in units b. Within the D8 void obstacle family, data points are colored by void fraction F. (For interpretation of the references to color in this figure legend, the reader is referred to the web version of this article.)

4.2.2. ISFE/USFE ratio

The analysis thus far has shown nanovoid strengthening τ_c has a geometric component, F, and a constant material component M, which affects the scaling between τ_c and F, i.e.,

$$\frac{\tau_c}{\mu} = MF \tag{21}$$

It has also been made clear that no one material property dominates τ_c influence, as evidenced by weak to moderate trends with both ISFE and SFW in Fig. 7, although μ and the dislocation core structure play a role.

Our results suggest τ_c scales with F for all metals when M follows:

$$M = \alpha\left(\frac{ISFE}{USFE} + \beta\right). \tag{22}$$

where α and β are coefficients that provide the best fit to this linear trend, with α taken as approximately $1/100$ and β as $\pi/4$. As a first attempt to identify operative material properties, the finding points to $ISFE/USFE$ as the influential property of the material γ-surface, and effective moduli μ as the other dominant material property. The level of agreement between our simulation results and Eqs. (21) and (22) can be seen from Fig. 8.

Eqs. (21) and (22), named the Linear Fraction (LF) model, predict the relationship between the critical stress and void F for all metals in Fig. 8, with the exception of the two smallest voids in Pt. Beyond PFDD, the LF model captures very well the relationship in critical stress versus void F for dislocations with low SFE values as predicted by atomistic simulation (Asari et al., 2013) in Fig. 9. This series of pseudo-SFE MD studies (Doihara et al., 2018; Okita et al., 2014; Asari et al., 2013) investigated the influence of dissociation on nanovoid strengthening by discretely varying the SFE value of a base material with a parent structure set by the Cu EAM (Embedded Atom Method) interatomic potential. As discussed in the Introduction, MD literature is limited in the number of reliable EAM potentials for fcc materials, and as a result a sweeping study of nanovoid strengthening across different fcc materials

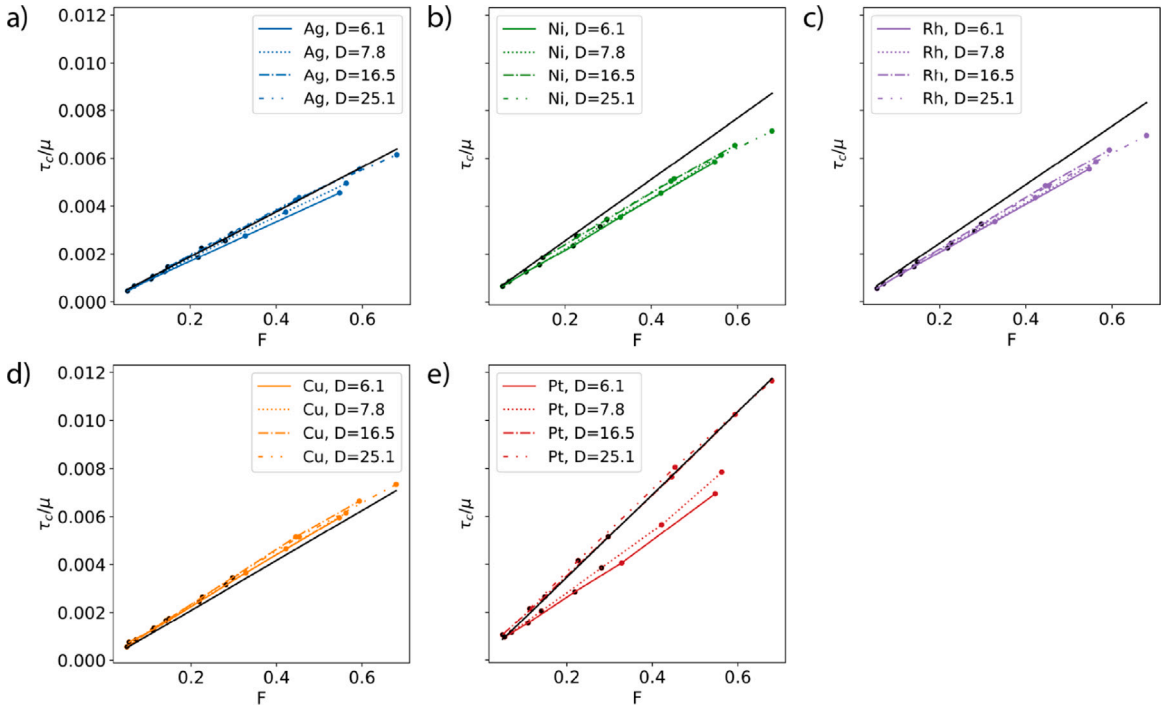

Fig. 8. Breakdown of comparison between predictive slope from Eqs. (21) and (22), forming the LF model, and PFDD calculations. All five materials are plotted in color from (a)-(e), with the predictive equation in black. (For interpretation of the references to color in this figure legend, the reader is referred to the web version of this article.)

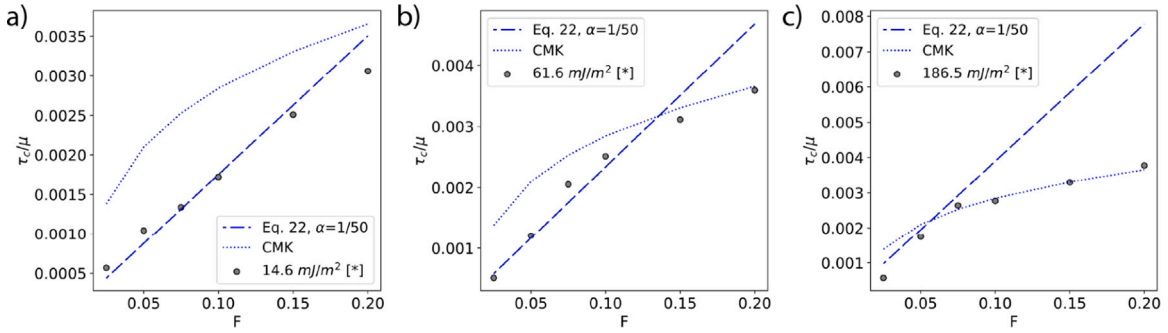

Fig. 9. A comparison is given between Eqs. (21) and (22), analytical trends as predicted by the CMK model (Crone et al., 2015), and the 100K MD study of the influence of SFE on nanovoid strengthening through the pseudo-SFE technique, where [*] indicates reference to Asari et al. (2013).

would introduce additional uncertainties in results due to the varying quality of these material inputs. It is important to note that these MD studies have isolated the influence of SFE on nanovoid strengthening, while USFE is held constant and the additional effects of elastic constants (and resulting elastic anisotropy), shear modulus, and Burgers vector that accompany different materials are not taken into account.

With this PFDD study enabling a more complete investigation into material and void size effects on strengthening than was available in MD, we are able to identify a key transition for fcc metals. Fig. 9 shows three representative SFE cases from Asari et al. (2013) plotted together with our LF model and the analytical CMK model, which does not change from Fig. 9a-c. Two remarkable phenomena are identified: first, this LF model is capable of predicting nanovoid strengthening for fcc metals in atomistics, and second, a transition in strengthening trends exists and is dependent on material SFE. The MD data follows the LF model at low to moderate SFE and the CMK model at high SFE values. Only for the highest SFE value and higher void F values is the CMK model the more effective descriptor, which may be due to the fact that the dislocation is assumed to be perfect and not extended in the SB and CMK models, as it is in the PFDD and atomistic calculations. Dissociation has a measurable impact on strengthening trends, and while SFE alone does not strongly influence obstacle strength, it contributes substantially in the context of the ISFE/USFE ratio.

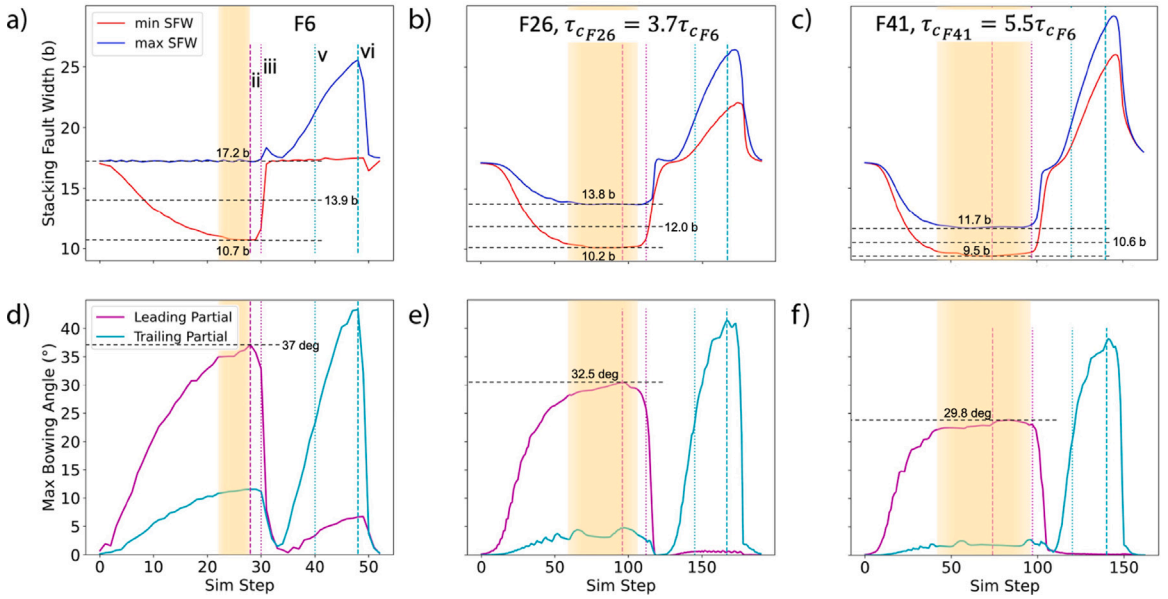

Fig. 10. Variation in shearing behavior for representative case of Cu for void fractions F6, F26, and F41 for void size D8. Approximate crawling regions are shaded, and one should note the different x-axis scalings between void fractions.

4.3. Shearing response

4.3.1. Controlling mechanism in light of prior theories and simulations

To understand the mechanisms behind the remarkable linear trend captured by the LF model seen in Fig. 9, we analyze the dominant factors at play for the critical step which determines τ_c. First, the critical step for τ_c in this study is observed to be the crawling period before the dislocation pierces the void, and τ_c is set by the leading partial impingement stress. This is the case for all void geometries and all materials (including Pt_{Cu}) except Pt. Below τ_c, when under-driven, the dislocation arrests at a finite distance from the void surface. At an applied stress of τ_c, the leading and trailing partial dislocations are able to glide towards the voids, but at a slow and steady pace during the crawling period. This ends when the leading partial moves within the capture radius from the void surface, where image forces dominate and draw the partial to the void. After this point, no further increment in stress is needed for the leading and trailing partials to sequentially shear the void, straighten, and restore their initial SFW.

This critical step in PFDD deviates from what has been reported previously in analytical models for undissociated dislocations, and with MD for dissociated Cu dislocations. Line tension models, such as the SB and CMK models (Scattergood and Bacon, 1982; Crone et al., 2015), on the other hand, associate τ_c with the stress for the dislocation to breakaway away from the void after initially and partially cutting it. These models evolved from those originally developed to understand compact, undissociated dislocation interactions with weak precipitates. Key parameters relating this critical stress to void dimensions are the penetration depth for the dislocation and the angle of incidence at the immediate void surface. As dislocations cannot exist inside voids, the penetration depth in the case of a void refers to the distance between the point of intersection of the dislocation line with the void surface and the void array centerline. For these models, the incidence angle at this intersection point is measured from the direction normal to the void array centerline. After the dislocation has partially penetrated the void, a higher τ_c corresponds to lower incidence angles, which brings it closer to the Orowan shearing mode (Scattergood and Bacon, 1975) for impenetrable obstacles. We also recall that the dislocation configuration in cases reported from MD take on a different geometry than at the critical step in this study. In Hatano and Matsui (2005), Osetsky and Bacon (2005), Simar et al. (2011), the dislocation configuration at maximum applied stress mirrors that of the analytical models in principle, with dislocation segments that pierce neighboring void surfaces while bowing out in the material space between obstacles. However, Fig. 9 confirms that these minute differences at the void surface are not controlling τ_c, with Asari et al. (2013), Doihara et al. (2018) studies following nicely with the LF model for low SFE materials. In other words, the controlling mechanism for τ_c is unrelated to these configurational differences.

We propose that τ_c is associated with the critical stress to constrict the SFW below its dynamic value in the presence of an obstacle. In Fig. 10, for the case of Cu with D held constant and F increasing from 6% to 41%, the maximum and minimum SFW and bow angles along the dislocation line are tracked in time as the dislocation intersects the voids. These sequences occur at the corresponding τ_c and follow the dislocation from the beginning, on approach, to the end after it shears the voids. The crawling period has been highlighted in yellow, with minimum, maximum, and average SFW reported in this range. As F increases, we find that τ_c increases five fold while both the average SFW and the leading partial bowing angle decrease. Conventional models (Scattergood and Bacon, 1982) would instead associate the increase in D/S and consequential decrease in maximum bowing angle with a decrease in τ_c, which is not observed even when normalizing τ_c by the relevant factor used in the SB model. Instead, this decrease in average

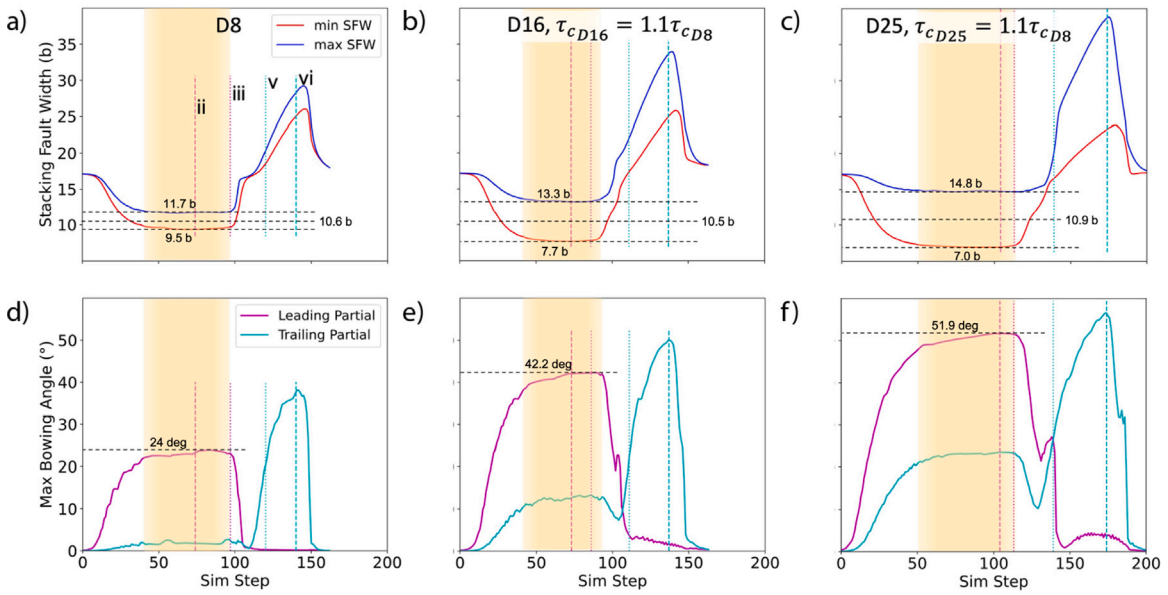

Fig. 11. Variation in shearing behavior for a representative case of Cu for void sizes D8, D16, and D25 for nominal void fractions F41. For D8F41 the actual void fraction is 42.2%, for D16F41 the actual fraction is $F = 44.5\%$, and for D25F41 the actual fraction is $F = 45.3\%$. Approximate crawling regions are shaded.

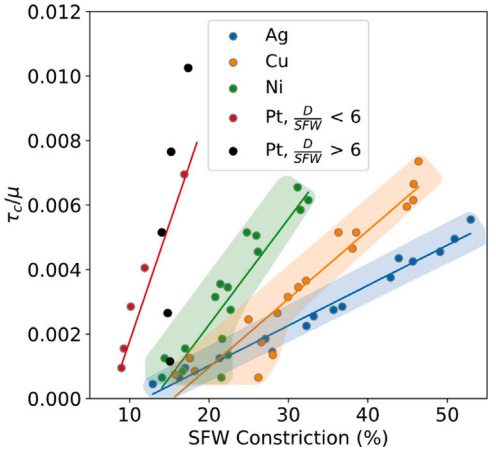

Fig. 12. Relationship between τ_c and the average SFW constriction in percent along the entire dislocation line as it bows around the void obstacle in the crawling period. All materials but Rh are represented, which behaves very similarly to Ni. Linear regression curves are plotted and scatter regions highlighted to illustrate a slight broadening at lower SFW constriction, correlating with higher D, lower F cases. Pt is segmented into two data sets, with a regression line for lower D/SFW ratio values, and higher D/SFW ratios showing a nearly constant SFW constriction for all τ_c.

SFW, which can also be considered an increase in average SF constriction along the dislocation line, is linearly correlated with the increase in τ_c. The other cases not shown follow a similar trend.

Fig. 11 shows the complementary case for Cu of varying D values, and F values nearly fixed at the target value of 41%. Within the crawling period, again highlighted in yellow, the maximum and minimum values of the instantaneous SFW evolve with D, but the average SFW constriction is held constant while F is held constant. In contrast, the bowing angles of both leading and trailing partials increase substantially with D. For these three cases, τ_c only mildly varies, much like the small variations in actual F in relation to target F values. Clearly τ_c does not correlate with the substantial changes in bowing angles of the partials in either Fig. 10 or Fig. 11, as would be expected from the simplified compact dislocation SB and CMK models. Taken together, Figs. 10 and 11 make a case for average SFW constriction as the critical step determining the obstacle critical stress. This is a feature both PFDD and MD can be expected to capture, and hence would explain why estimates of τ_c from both follow the LF model.

In Fig. 12, τ_c is plotted as a function of the amount of SFW constriction averaged along the dislocation as it bows at the critical step, i.e., the crawling period, for all materials and void geometries tested in this study (excluding Rh, which behaves very similarly to Ni). A compelling linear relationship is observed across non-Pt materials and void sizes, with a possible increase in spread for

small SF constriction in cases with larger void sizes and low F. Considering Figs. 9–12, the results of our calculations suggest that translating the analytical models from perfect dislocations to extended ones may not be appropriate for low SFE materials, and that our LF model may instead be the preeminent trend for these cases.

4.3.2. Platinum size effect influenced by shift in critical shearing stage

The outlier to the aforementioned shearing behavior is Pt. In Pt, the dislocation glides approximately as a perfect dislocation. In Fig. 4, the leading and trailing partials behave nearly identically at each step in the sequence. Further, throughout the interaction with the nanovoids, the SFW along the length of the extended dislocation line varies by only $\approx 1b$ in Fig. 4a and 4d.

These differences in Pt from the other cases manifest as a void size, D, dependence. For smaller voids, D6 and D8, the void diameter is a few times that of the SFW. At sub-critical stresses, the dislocations stop short of the void surface. As in the other metals, this is the critical configuration controlling τ_c, except here both partials are involved instead of just the leading partial. The bypass mechanism for larger D in Pt is similar to that anticipated by analytical models, which treat a perfect dislocation, because we see the dislocation begin to both bow out and pierce the void at the critical step. In the work of Crone et al. (2015), for sub-critical conditions, the dislocation pierced the voids and was pinned at an intermediate location without fully cutting them. An increase in external stress would bow the dislocations further until they could successfully shear the obstacle array.

Fig. 12 shows the distinction between small and large D datasets emerges in the case of Pt for SFW constriction as well. Low D/SFW values (< 6) show the same trend as observed with the other metals. τ_c increases linearly with the amount the SFW constricts when intersecting the voids. The only difference is that the already narrow Pt core constricts less than the other metals. At higher D/SFW cases (> 6), however, the amount the Pt SFW constricts becomes negligible and independent of void geometry. In these cases, the void diameters D16 and D25 are nearly an order of magnitude greater than the Pt SFW, approaching the limit in which the dislocation can be represented as an undissociated perfect dislocation cutting a void and constriction is negligible. No other metal studied here achieved this condition for the same range of nanovoid sizes. Yet still, the τ_c for Pt scales with F for the full range of D, even these larger sizes.

4.4. Nanovoid strengthening within the broader scope of strengthening mechanisms

The question remains: how does strength scaling revealed in this study relate to bulk behavior? One could use these trends to inform a strengthening model for fcc metals with slip strengths related to local nanovoid density. The one dimensional void fraction F can be geometrically related to void densities of local void clusters in two- and three-dimensions, according to:

$$\begin{aligned} F_{2D} &= \frac{\pi}{4} F^2. \\ F_{3D} &= \frac{\pi}{6} F^3. \end{aligned} \tag{23}$$

From the F6 to the F60 void fraction groups in this study, the localized 2D void obstacle densities range between 0.3% and nearly 30%. Increasing the dimensionality of the problem further, the localized 3D void obstacle density ranges between 0.01% to around 10%. It is an open question which extrapolated density, 2D or 3D, is more relevant to experiment. As obstacles to shearing, a 2D void density may be relevant to slip within a single plane. As a more complex network of microstructural obstacles, the 3D density may be relevant if multiple slip systems are active or dislocations are being distorted and pinned due to other defects in this localized region of high void density, causing them to interact with the nanovoids more through a 3D volume than a 2D plane.

A case study on the appropriate dimensionality of F can be done by comparing these results with those of irradiated austenitic stainless steels (Lucas, 1993). For neutron irradiation at elevated temperatures in austenitic stainless steels, which are expected to have SFE values (Schramm and Reed, 1975; Bampton et al., 1978) anywhere between those for Ag and Cu used in the present study, a localized volumetric void density of up to 8%–9% was observed at doses of 10dpa assuming a void diameter of 20 nm. At this dosage, an associated increase in yield stress is observed between 3 and 5 fold from the expected response of the pristine material. These yield stresses include influences from all irradiation-induced microstructural defects present, of which nanovoids are important contributors.

For our study, the sensitivity to relative local void densities varies significantly across the five fcc metals. At the correlated 3D void density of 11% (from the F60 data), our calculations show that Ag strengthening scales to over 100 fold increase from $\tau_{peierls}$, while Cu scales to nearly 20 fold increase from $\tau_{peierls}$. For reference, Pt sees over 10 fold increase from $\tau_{peierls}$. Clearly the 3D void density overestimates the strengthening effects for localized high-density nanovoid obstacles by an order of magnitude compared to results obtained by Lucas (1993). Reducing the void density to the calculated 2D values, the F26 grouping corresponds to a 2D density of 5%, while the F41 grouping scales to a 2D void density of 13%. Between these two densities, the PFDD calculations show a 50–75 fold increase in τ_c from $\tau_{peierls}$ for Ag and a 8–13 fold increase from $\tau_{peierls}$ in Cu. These strengthening trends follow more closely with experimental austenitic stainless steel values (Lucas, 1993); some of the over-estimation could be attributed to the relatively large void diameters in the experimental data (20 nm) compared to the voids in this study (≈1-–7 nm).

Additionally, it is important to differentiate the nanovoid strengthening in this work from any subsequent hardening response. A point was made by Scattergood and Bacon (1982) that voids do not act as effective dislocation density multipliers because no loops are left encircling them after shearing, and thus initial yield strength may be increased but work hardening behavior analogous to what is seen in precipitate hardening is not expected. In fact, the strengthening effect of nanovoids actually decreases once they are sheared by a dislocation, as seen for fcc (Xu et al., 2019a) and bcc (Yu et al., 2022). So, while nanovoids may have the effect

of increasing bulk yield strength, they also may contribute to a reduction in bulk hardening, or even bulk strain softening, during loading.

Lastly, Scattergood and Bacon suggested nanovoids are strong obstacles similar to impenetrable obstacles, while Crone Munday and Knapp corrected these values down but still largely overestimated the obstacle stresses for voids in Fig. 6. This question has been explored by Xu et al. (2022a), where it was found that shearable voids, such as those in this study, were the weakest of all obstacles by a factor of nearly 1.5 for the tightest obstacle spacing, and shearable precipitates and voids were both weaker than impenetrable precipitates and voids, respectively. However, as obstacle spacing was increased the difference in bypass stress between the type of obstacles became negligible, meaning voids and unshearable precipitates both acted as identical obstacles at low volume fractions, suggesting a sensitivity to obstacle volume fraction that could not have been predicted by either the CMK or the SB model. These disagreements between analytical trends and previous PFDD results help explain the continued inability of current analytical models to approximate both the orders of magnitude and the observed spread in critical obstacle stresses for nanovoids.

Taking the technique as a whole, PFDD maintains the position held in literature that nanovoids in fcc are potent strengtheners, if not as strong as unshearable inclusions. Future work with this technique can consider a number of complexities that PFDD is well suited to explore, including either the geometric distribution of nanovoid obstacles in 2D and 3D, or the influence of temperature on the sensitivity of this work to both SFE and ISFE/USFE material properties. The incorporation of temperature into PFDD has recently been achieved in Albrecht et al. (2023).

5. Conclusions

Many materials of interest for nuclear power applications have fcc cubic structure. After irradiation, nanovoids can form in local regions of the material, greatly affecting their deformation behavior, such as yield strength and strain hardening behavior. The underlying mechanism has been associated with the interaction of these voids with moving dislocations, since their length scales are comparable. In this work, a phase field dislocation dynamics (PFDD) model was used to study the interaction of extended dislocations in many fcc metals with a local array of nanovoids. The PFDD model is a mesoscale model that predicts the minimum energy pathway taken as the dislocation shears the voids. In this framework, the entire *ab initio* calculated γ-surface is imported and the full anisotropic elastic tensor is used. As such, dislocation cores are dissociated into two Shockley partials with a stacking fault in between. The diameters and spacings among the nanovoid array varied respectively from $6b$ to $25b$ and from $5b$ to $\approx 300b$, where b is the value of the Burgers vector of the metal. Both the critical stress τ_c to bypass the array and the critical stage that controls it are investigated. The main findings from this study are given below.

- The critical stress τ_c is controlled by the stress needed for the leading partial to impinge the void. It is required to push the leading partial within the capture radius, where it is attracted to the void. This condition applies to most metals and local nanovoid concentrations tested, with very few exceptions.
- When dislocation bypass is controlled by the leading partial impingement stress, τ_c directly scales with the linear void fraction rather than exhibiting individual dependencies on void size or void spacing. A best fit Linear Fraction (LF) model is constructed from the calculations.
- Regarding the role of material properties, τ_c scales linearly with the ratio of the unstable and intrinsic stacking fault energies and the shear modulus.
- For low SFE values, as many fcc metals have, nanovoid strengthening trends follow the LF model well. From comparison with atomistics, a transition to more closely following analytical model trends is expected at high SFE values.
- When the void diameter is an order of magnitude larger than the width of the dislocation core, the critical stress is determined by the stress for the dislocation to breakaway from the void after it has partially sheared it. This bypass mechanism is similar to the conventional case, anticipated by line tension models and observed in atomistic simulations. Here this situation manifests with Pt, which has a very fine core ($\sim$ 1 nm), and the relatively larger nanovoid sizes tested.

CRediT authorship contribution statement

Ashley M. Roach: Visualization, Formal analysis, Investigation, Writing – original draft. **Shuozhi Xu:** Methodology, Software, Writing – review & editing. **Darby J. Luscher:** Writing – review & editing, Supervision. **Daniel S. Gianola:** Writing – review & editing, Supervision. **Irene J. Beyerlein:** Conceptualization, Methodology, Writing – review & editing, Supervision.

Declaration of competing interest

The authors declare that they have no known competing financial interests or personal relationships that could have appeared to influence the work reported in this paper.

Data availability

Data will be made available on request.

Acknowledgments

A.M.R. would like to acknowledge support of the DOE NNSA LRGF fellowship, the joint collaboration with Los Alamos National Laboratory (LANL), and the cooperative agreement DE-NA0003960 that supports the DOE NNSA LRGF. I. J. B. would like to acknowledge support from the Office of Naval Research, United States under contract N00014-21-1-2536. D.J.L. is grateful for the support of the Advanced Simulation and Computing, Physics and Engineering Models program at Los Alamos National Laboratory, United States. Use was made of computational facilities purchased with funds from the National Science Foundation, United States (No. CNS-1725797) and administered by the Center for Scientific Computing (CSC). The CSC is supported by the California NanoSystems Institute and the Materials Research Science and Engineering Center (MRSEC; No. NSF DMR 1720256) at UC Santa Barbara.

References

Albrecht, C., Beyerlein, I.J., Jones, M.R., 2023. Temperature dependent phase field dislocation dynamics model. Eur. J. Mech. A Solids 100, 104987. http://dx.doi.org/10.1016/j.euromechsol.2023.104987.

Anderson, P.M., Hirth, J.P., Lothe, J., 2017. Theory of Dislocations. Cambridge University Press.

Asari, K., Hetland, O., Fujita, S., Itakura, M., Okita, T., 2013. The effect of stacking fault energy on interactions between an edge dislocation and a spherical void by molecular dynamics simulations. J. Nucl. Mater. 442 (1), 360–364. http://dx.doi.org/10.1016/j.jnucmat.2013.05.076.

Bacon, D.J., Osetsky, Y.N., 2005. Modelling dislocation–obstacle interactions in metals exposed to an irradiation environment. Mater. Sci. Eng. A 400, 353–361. http://dx.doi.org/10.1016/j.msea.2005.01.061.

Bampton, C., Jones, I., Loretto, M., 1978. Stacking fault energy measurements in some austenitic stainless steels. Acta Metall. 26 (1), 39–51. http://dx.doi.org/10.1016/0001-6160(78)90200-6.

Bao, Q., Huang, M., Zhu, Y., Zhao, L., Li, Z., 2022. Abnormal interactions between high-speed edge dislocation and microvoid in BCC metals. Int. J. Plast. 148, 103125. http://dx.doi.org/10.1016/j.ijplas.2021.103125.

Bergner, F., Gillemot, F., Hernández-Mayoral, M., Serrano, M., Török, G., Ulbricht, A., Altstadt, E., 2015. Contributions of cu-rich clusters, dislocation loops and nanovoids to the irradiation-induced hardening of cu-bearing low-Ni reactor pressure vessel steels. J. Nucl. Mater. 461, 37–44. http://dx.doi.org/10.1016/j.jnucmat.2015.02.031.

Beyerlein, I., Hunter, A., 2016. Understanding dislocation mechanics at the mesoscale using phase field dislocation dynamics. Phil. Trans. R. Soc. A 374 (2066), 20150166. http://dx.doi.org/10.1098/rsta.2015.0166.

Chen, C., Song, J., 2022. A combined atomistic-continuum study on the unfaulting of single and multi-layer interstitial dislocation loops in irradiated FCC and HCP metals. Int. J. Plast. 152, 103231. http://dx.doi.org/10.1016/j.ijplas.2022.103231.

Christodoulou, P.G., Dancette, S., Lebensohn, R.A., Maire, E., Beyerlein, I.J., 2021. Role of crystallographic orientation on intragranular void growth in polycrystalline FCC materials. Int. J. Plast. 147, 103104. http://dx.doi.org/10.1016/j.ijplas.2021.103104.

Crone, J., Munday, L., Knap, J., 2015. Capturing the effects of free surfaces on void strengthening with dislocation dynamics. Acta Mater. 101, 40–47. http://dx.doi.org/10.1016/j.actamat.2015.08.067.

Dérès, J., Proville, L., Marinica, M.C., 2015. Dislocation depinning from nano-sized irradiation defects in a bcc iron model. Acta Mater. 99, 99–105. http://dx.doi.org/10.1016/j.actamat.2015.07.067.

Doihara, K., Okita, T., Itakura, M., Aichi, M., Suzuki, K., 2018. Atomic simulations to evaluate effects of stacking fault energy on interactions between edge dislocation and spherical void in face-centred cubic metals. Phil. Mag. 98 (22), 2061–2076. http://dx.doi.org/10.1080/14786435.2018.1472401.

Eghtesad, A., Germaschewski, K., Beyerlein, I.J., Hunter, A., Knezevic, M., 2018. Graphics processing unit accelerated phase field dislocation dynamics: Application to bi-metallic interfaces. Adv. Eng. Softw. 115, 248–267. http://dx.doi.org/10.1016/j.advengsoft.2017.09.010.

Fan, J., Ji, X., Fu, L., Wang, J., Ma, S., Sun, Y., Wen, M., Shan, A., 2022. Achieving exceptional strength-ductility synergy in a complex-concentrated alloy via architected heterogeneous grains and nano-sized precipitates. Int. J. Plast. 157, 103398. http://dx.doi.org/10.1016/j.ijplas.2022.103398.

Fukuda, M., Kiran Kumar, N., Koyanagi, T., Garrison, L.M., Snead, L.L., Katoh, Y., Hasegawa, A., 2016. Neutron energy spectrum influence on irradiation hardening and microstructural development of Tungsten. J. Nucl. Mater. 479, 249–254. http://dx.doi.org/10.1016/j.jnucmat.2016.06.051.

Hatano, T., Matsui, H., 2005. Molecular dynamics investigation of dislocation pinning by a nanovoid in copper. Phys. Rev. B 72 (9), 094105. http://dx.doi.org/10.1103/PhysRevB.72.094105.

Hayakawa, S., Doihara, K., Okita, T., Itakura, M., Aichi, M., Suzuki, K., 2019. Screw dislocation–spherical void interactions in fcc metals and their dependence on stacking fault energy. J. Mater. Sci. 54, 11509–11525. http://dx.doi.org/10.1007/s10853-019-03716-0.

Hirsch, P.B., Kelly, A., 1965. Stacking-fault strengthening. Phil. Mag. A J. Theor. Exp. Appl. Phys. 12 (119), 881–900. http://dx.doi.org/10.1080/14786436508228118.

Huang, Y., Wiezorek, J., Garner, F., Freyer, P., Okita, T., Sagisaka, M., Isobe, Y., Allen, T., 2015. Microstructural characterization and density change of 304 stainless steel reflector blocks after long-term irradiation in EBR-II. J. Nucl. Mater. 465, 516–530. http://dx.doi.org/10.1016/j.jnucmat.2015.06.031.

Hunter, A., Beyerlein, I.J., Germann, T.C., Koslowski, M., 2011. Influence of the stacking fault energy surface on partial dislocations in fcc metals with a three-dimensional phase field dislocations dynamics model. Phys. Rev. B 84, 144108. http://dx.doi.org/10.1103/PhysRevB.84.144108, URL: https://link.aps.org/doi/10.1103/PhysRevB.84.144108.

Hunter, A., Zhang, R., Beyerlein, I., 2014. The core structure of dislocations and their relationship to the material γ-surface. J. Appl. Phys. 115, 134314. http://dx.doi.org/10.1063/1.4870462.

Lei, L., Marin, J.L., Koslowski, M., 2013. Phase-field modeling of defect nucleation and propagation in domains with material inhomogeneities. Modelling Simul. Mater. Sci. Eng. 21 (2), 025009. http://dx.doi.org/10.1088/0965-0393/21/2/025009.

Li, N., Demkowicz, M., Mara, N., Wang, Y., Misra, A., 2016. Hardening due to interfacial He bubbles in nanolayered composites. Mater. Res. Lett. 4 (2), 75–82. http://dx.doi.org/10.1080/21663831.2015.1110730.

Li, N., Nastasi, M., Misra, A., 2012. Defect structures and hardening mechanisms in high dose helium ion implanted Cu and Cu/Nb multilayer thin films. Int. J. Plast. 32–33, 1–16. http://dx.doi.org/10.1016/j.ijplas.2011.12.007.

Liu, S.M., Beyerlein, I.J., Han, W.Z., 2020. Two-dimensional vacancy platelets as precursors for basal dislocation loops in hexagonal zirconium. Nature Commun. 11 (1), 5766. http://dx.doi.org/10.1038/s41467-020-19629-5.

Liu, J., Huang, M., Li, Z., Zhao, L., Zhu, Y., 2021. Microvoid growth mechanism in FCC polycrystals and a statistical damage model. Int. J. Plast. 137, 102888. http://dx.doi.org/10.1016/j.ijplas.2020.102888.

Lucas, G., 1993. The evolution of mechanical property change in irradiated austenitic stainless steels. J. Nucl. Mater. 206 (2), 287–305. http://dx.doi.org/10.1016/0022-3115(93)90129-M.

Okita, T., Asari, K., Fujita, S., Itakura, M., 2014. Effect of the stacking fault energy on interactions between an edge dislocation and a spherical void in FCC metals at various spatial geometries. Fusion Sci. Technol. 66 (1), 289–294. http://dx.doi.org/10.13182/FST13-756.

Osetsky, Y., Bacon, D., 2005. Comparison of void strengthening in fcc and bcc metals: large-scale atomic-level modelling. Mater. Sci. Eng. A 400, 374–377. http://dx.doi.org/10.1016/j.msea.2005.02.083.

Osetsky, Y.N., Bacon, D.J., 2010. Atomic-scale mechanisms of void hardening in bcc and fcc metals. Phil. Mag. 90 (7–8), 945–961. http://dx.doi.org/10.1080/14786430903164580.

Peierls, R., 1940. The size of a dislocation. Proc. Phys. Soc. 52 (1), 34–37. http://dx.doi.org/10.1088/0959-5309/52/1/305.

Scattergood, R., Bacon, D., 1975. The orowan mechanism in anisotropic crystals. Phil. Mag. 31 (1), 179–198. http://dx.doi.org/10.1080/14786437508229295.

Scattergood, R., Bacon, D., 1982. The strengthening effect of voids. Acta Metall. 30, 1665–1677. http://dx.doi.org/10.1016/0001-6160(82)90188-2.

Schoeck, G., 2001. The core structure, recombination energy and Peierls energy for dislocations in Al. Phil. Mag. A 81 (5), 1161–1176. http://dx.doi.org/10.1080/01418610108214434.

Schramm, R., Reed, R., 1975. Stacking fault energies of seven commercial austenitic stainless steels. Metall. Trans. A 6, 1345–1351. http://dx.doi.org/10.1007/BF02641927.

Sills, R.B., Boyce, B.L., 2020. Void growth by dislocation adsorption. Mater. Res. Lett. 8 (3), 103–109. http://dx.doi.org/10.1080/21663831.2019.1702114.

Simar, A., Voigt, H.J.L., Wirth, B.D., 2011. Molecular dynamics simulations of dislocation interaction with voids in nickel. Comput. Mater. Sci. 50 (5), 1811–1817. http://dx.doi.org/10.1016/j.commatsci.2011.01.020.

Singh, B., Evans, J., 1995. Significant differences in defect accumulation behaviour between fcc and bcc crystals under cascade damage conditions. J. Nucl. Mater. 226 (3), 277–285. http://dx.doi.org/10.1016/0022-3115(95)00121-2.

Skoczeń, B., Ustrzycka, A., 2016. Kinetics of evolution of radiation induced micro-damage in ductile materials subjected to time-dependent stresses. Int. J. Plast. 80, 86–110. http://dx.doi.org/10.1016/j.ijplas.2016.01.006, URL: https://www.sciencedirect.com/science/article/pii/S0749641916000164.

Su, Y., Xu, S., Beyerlein, I.J., 2019. Density functional theory calculations of generalized stacking fault energy surfaces for eight face-centered cubic transition metals. J. Appl. Phys. 126, 105112. http://dx.doi.org/10.1063/1.5115282.

Voigt, W., 1889. Ueber die beziehung zwischen den beiden elasticitätsconstanten isotroper körper. Ann. Phys. 274, 573–587. http://dx.doi.org/10.1002/andp.18892741206.

Wang, M., Beyerlein, I.J., Zhang, J., Han, W.Z., 2018. Defect-interface interactions in irradiated Cu/Ag nanocomposites. Acta Mater. 160, 211–223. http://dx.doi.org/10.1016/j.actamat.2018.09.003.

Wang, M., Beyerlein, I.J., Zhang, J., Han, W.Z., 2019. Bi-metal interface-mediated defects distribution in neon ion bombarded Cu/Ag nanocomposites. Scr. Mater. 171, 1–5. http://dx.doi.org/10.1016/j.scriptamat.2019.06.016.

Warlimont, H., Martienssen, W., 2018. Springer Handbook of Materials Data. Springer.

Wen, Y.N., Zhang, J.M., 2007. Surface energy calculation of the fcc metals by using the MAEAM. Solid State Commun. 144 (3), 163–167. http://dx.doi.org/10.1016/j.ssc.2007.07.012.

Wu, K., Liu, G., Yu, P., Ye, C., Shi, J., Shen, Y., 2022. Prediction of hardening effect by irradiation-induced vacancy clusters with dislocation dynamics. Int. J. Plast. 149, 103160. http://dx.doi.org/10.1016/j.ijplas.2021.103160.

Xiong, L., Xu, S., McDowell, D.L., Chen, Y., 2015. Concurrent atomistic–continuum simulations of dislocation–void interactions in fcc crystals. Int. J. Plast. 65, 33–42. http://dx.doi.org/10.1016/j.ijplas.2014.08.002.

Xu, S., 2022. Recent progress in the phase-field dislocation dynamics method. Comput. Mater. Sci. 210, 111419. http://dx.doi.org/10.1016/j.commatsci.2022.111419.

Xu, S., Cheng, J.Y., Li, Z., Mara, N.A., Beyerlein, I.J., 2022a. Phase-field modeling of the interactions between an edge dislocation and an array of obstacles. Comput. Methods Appl. Mech. Engrg. 389, 114426. http://dx.doi.org/10.1016/j.cma.2021.114426, URL: https://www.sciencedirect.com/science/article/pii/S0045782521006691.

Xu, S., Cheng, J.Y., Mara, N.A., Beyerlein, I.J., 2022b. Dislocation dynamics in heterogeneous nanostructured materials. J. Mech. Phys. Solids 168, 105031. http://dx.doi.org/10.1016/j.jmps.2022.105031.

Xu, S., McDowell, D.L., Beyerlein, I.J., 2019a. Sequential obstacle interactions with dislocations in a planar array. Acta Mater. 174, 160–172. http://dx.doi.org/10.1016/j.actamat.2019.05.030, URL: https://www.sciencedirect.com/science/article/pii/S135964541930312X.

Xu, S., Mianroodi, J.R., Hunter, A., Beyerlein, I.J., Svendsen, B., 2019b. Phase-field-based calculations of the disregistry fields of static extended dislocations in FCC metals. Phil. Mag. 99 (11), 1400–1428. http://dx.doi.org/10.1080/14786435.2019.1582850.

Xu, S., Mianroodi, J.R., Hunter, A., Svendsen, B., Beyerlein, I.J., 2020a. Comparative modeling of the disregistry and Peierls stress for dissociated edge and screw dislocations in Al. Int. J. Plast. 102689. http://dx.doi.org/10.1016/j.ijplas.2020.102689, URL: http://www.sciencedirect.com/science/article/pii/S0749641919303808.

Xu, S., Smith, L., Mianroodi, J.R., Hunter, A., Svendsen, B., Beyerlein, I.J., 2019c. A comparison of different continuum approaches in modeling mixed-type dislocations in Al. Modelling Simul. Mater. Sci. Eng. 27 (7), 074004. http://dx.doi.org/10.1088/1361-651X/ab2d16.

Xu, S., Su, Y., Beyerlein, I.J., 2019d. Modeling dislocations with arbitrary character angle in face-centered cubic transition metals using the phase-field dislocation dynamics method with full anisotropic elasticity. Mech. Mater. 139, 103200. http://dx.doi.org/10.1016/j.mechmat.2019.103200.

Xu, A., Wei, T., Bhattacharyya, D., 2020b. The effect of strain rate and orientation on he ion irradiated Ni single crystals – An in situ micro-tensile study. Int. J. Plast. 126, 102627. http://dx.doi.org/10.1016/j.ijplas.2019.11.006.

Yu, P., Liu, G., Wu, K., Cui, Y., Zhao, G., Shen, Y., 2022. Exploring the effects of the sheared voids on the hardening of tungsten using atomistic simulations. J. Nucl. Mater. 562, 153548. http://dx.doi.org/10.1016/j.jnucmat.2022.153548, URL: https://www.sciencedirect.com/science/article/pii/S0022311522000447.

Zeng, Y., Cai, X., Koslowski, M., 2019. Effects of the stacking fault energy fluctuations on the strengthening of alloys. Acta Mater. 164, 1–11. http://dx.doi.org/10.1016/j.actamat.2018.09.066.

Zinkle, S., Matsukawa, Y., 2004. Observation and analysis of defect cluster production and interactions with dislocations. J. Nucl. Mater. 329–333, 88–96. http://dx.doi.org/10.1016/j.jnucmat.2004.04.298, Proceedings of the 11th International Conference on Fusion Reactor Materials (ICFRM-11).